doi.org/10.26434/chemrxiv.5845635.v1

CO2 and Water Activation on Ceria Nanocluster Modified TiO2 Rutile (110)

Michael Nolan, Stephen Rhatigan

Submitted date: 01/02/2018 • Posted date: 02/02/2018

Citation information: Nolan, Michael; Rhatigan, Stephen (2018): CO2 and Water Activation on Ceria Nanocluster Modified TiO2 Rutile (110). ChemRxiv. Preprint.

Surface modification of TiO_2 with metal oxide nanoclusters is a strategy for the development of new photocatalyst materials. We have studied modification of the (110) surface of rutile TiO_2 with ceria nanoclusters using density functional theory corrected for on-site Coulomb interactions (DFT+U). We focus on the impact of surface modification on key properties governing the performance of photocatalysts, including light absorption, photoexcited charge carrier separation, reducibility and surface reactivity. Our results show that adsorption of the CeO_2 nanoclusters, with compositions Ce_5O_{10} and Ce_6O_{-12}, is favourable at the rutile (110) surface and that the nanocluster-surface composites favour non-stoichiometry in the adsorbed ceria so that reduced Ce ions will be present in the ground state. The presence of reduced Ce ions and low coordinated O sites in the nanocluster lead to the emergence of energy states in the energy gap of the TiO_2 host, which potentially enhance the visible light response. We show, through an examination of oxygen vacancy formation, that the composite systems are reducible with moderate energy costs. Photoexcited electrons and holes localize on Ce and O sites of the supported nanoclusters. The interaction of CO_2 and H_2O is favourable at multiple sites of the reduced CeO_x-TiO_2 composite surfaces. CO_2 adsorbs and activates, while H_2O spontaneously dissociates at oxygen vacancy sites.

File list (2)

CO_2 and Water Activation on Ceria Nanocluster Modified TiO_2 Rutile (110)

Stephen Rhatigan and Michael Nolan*

Tyndall National Institute, University College Cork, Lee Maltings, Cork, Ireland

*Corresponding author: michael.nolan@tyndall.ie

Abstract

Surface modification of TiO_2 with metal oxide nanoclusters is a strategy for the development of new photocatalyst materials. We have studied modification of the (110) surface of rutile TiO_2 with ceria nanoclusters using density functional theory corrected for on-site Coulomb interactions (DFT+U). We focus on the impact of surface modification on key properties governing the performance of photocatalysts, including light absorption, photoexcited charge carrier separation, reducibility and surface reactivity. Our results show that adsorption of the CeO_2 nanoclusters, with compositions Ce_5O_{10} and Ce_6O_{12}, is favourable at the rutile (110) surface and that the nanocluster-surface composites favour non-stoichiometry in the adsorbed ceria so that reduced Ce ions will be present in the ground state. The presence of reduced Ce ions and low coordinated O sites in the nanocluster lead to the emergence of energy states in the energy gap of the TiO_2 host, which potentially enhance the visible light response. We show, through an examination of oxygen vacancy formation, that the composite systems are reducible with moderate energy costs. Photoexcited electrons and holes localize on Ce and O sites of the supported nanoclusters. The interaction of CO_2 and H_2O is favourable at multiple sites of the reduced CeO_x-TiO_2 composite surfaces. CO_2 adsorbs and activates, while H_2O spontaneously dissociates at oxygen vacancy sites.

1 INTRODUCTION

Since the seminal paper by Fujishima and Honda in 1972,[1] titanium dioxide, TiO_2, has remained at the forefront of photocatalysis research due to its abundance, low-cost, non-toxicity and robustness under operating conditions. The large bandgap (>3 eV) means that TiO_2 is UV active so that extending light absorption to the visible range is necessary to maximize solar energy absorption for large-scale implementation of photocatalytic technologies.

Strategies to induce visible light absorption in TiO_2 have included substitutional cation or anion doping at Ti or O sites respectively[2-13] and co-doping, where multiple dopants are incorporated in the TiO_2 host.[12-20] Doping introduces impurity energy states into the band gap of the TiO_2 host, facilitating electronic transitions that have energies in the visible range. However, localized defect states have been shown to act as recombination centres, impeding carrier migration and reducing photocatalytic activity[9, 12, 13] and practical issues with reproducibility, solubility and stability persist with doped metal oxides.

Extending the absorption edge to longer wavelengths should not be the sole research focus as efficient separation of photoexcited charge carriers and molecular activation are essential to the performance of photocatalysts. The development of the dye sensitized solar cell (DSSC)[21] can inspire similar strategies in photocatalysis; dyes simultaneously promote visible light absorption and charge separation but do suffer from degradation.[13] Noble-metal loading of TiO_2 has been reported to improve photocatalytic efficiency in the UV and visible through plasmon resonance in the metal.[22-26] However, the use of precious metals such as Ag, Au and Pt drives up costs.

Surface modification of TiO_2 with dispersed metal oxide nanoclusters of non-precious metals has been investigated experimentally via chemisorption-calcination cycle (CCC)[27, 28] and atomic layer deposition (ALD).[29] These studies reported both band gap reduction and enhanced visible light photocatalytic activity for FeO_x-modified TiO_2. Photoluminescence spectroscopy revealed that the modification suppressed carrier recombination[27] and the observed red shift was due to cluster derived states above the valence band maximum (VBM) as identified by X-ray photoelectron spectroscopy (XPS) and confirmed with density functional theory (DFT) simulations.[27, 28, 30]

DFT has been used in combination with experiment to examine these and similar systems.[28, 30-43] Our previous work[28, 31, 34-40, 43, 44] has indicated the potential for metal oxide modifiers to induce a bandgap reduction over bare TiO_2. In addition, an enhanced separation of photoexcited electrons and holes has been reported to result from nanocluster surface modification of TiO_2.[34, 36, 37, 40, 45] We have further highlighted the role of low-coordinated nanocluster metal and/or oxygen sites in trapping and separating charge carriers[34, 36, 37, 40] and this suggests that modification of TiO_2 promotes electron and hole separation. Initial work on CO_2 activation at metal oxide modified TiO_2 has been presented.[31]

In this paper, we present a DFT study of TiO_2 rutile (110) modified with sub-nm nanoclusters of CeO_2, with specific compositions Ce_5O_{10} and Ce_6O_{12}. CeO_2 is an interesting modifier as Ce 4f states are crucial in optical properties, reducibility and reactivity.[46, 47] In particular, the facile conversion between Ce^{4+} and Ce^{3+} oxidation states has important implications for catalytic performance and metal/CeO_x/TiO_2 composites with Ce^{3+} cations have displayed enhanced activity for the water gas shift (WGS) reaction.[42, 48-50] We focus in particular on the impact of nanocluster modification on (1) the interfacial atomic structure, (2) the valence or conduction band edges of rutile (110), (3) charge localization after excitation, (4) the reducibility of the composite system and (5) the interaction of feedstock molecules, such as H_2O and CO_2, with

the reduced CeO_x-TiO_2 composite. Reducibility and interactions with molecules are crucial for catalysis. A more reducible catalyst could use a combination of photocatalytic and thermal catalytic effects.[51] Electrons and holes can be produced by light absorption and thermally produced defects, such as oxygen vacancies, can provide sites for the adsorption and activation of feedstock species.

Transition metal oxides have been widely studied as catalysts for the oxygen evolution reaction (OER).[52, 53] Nørskov and colleagues studied water oxidation at the rutile TiO_2 (110) surface using DFT[54] and found that the most difficult step was the dissociation of a H_2O molecule at a vacancy site to form an adsorbed hydroxyl group (OH*). Other DFT studies have examined water adsorption at extended surfaces of both rutile TiO_2 (110)[55] and CeO_2 (111)[56, 57] and found that molecular adsorption of water is more favourable than dissociative adsorption, albeit marginally so for the latter system (0.01-0.03 eV depending on exchange-correlation functional and separated by an energy barrier of 0.1 eV). A recent study compared water adsorption at the (101) (E_{ads} = 0.89 eV) and (001) (E_{ads} = 0.29 eV) surfaces of anatase TiO_2.[58] The authors attributed the greater activity of the (001) surface for water oxidation to hydrogen bonds between H_2O and terminal hydroxyls which facilitate rapid hole transfer. In general, the adsorption configuration of water molecules at TiO_2 surfaces depends on the crystal form, termination, stoichiometry and degree of coverage.[33, 59] However, an important first step, consistent across mechanisms describing water oxidation, is the dissociative adsorption of H_2O at the catalyst surface.[60-62] DFT+U studies examining ceria nanoclusters, of composition Ce_2O_3, supported on rutile (110) found that water dissociation is exothermic (E_{ads} = -0.7 eV) with a small energy barrier (0.04 eV).[42, 48] In addition, a number of studies have highlighted the role played by dissociated H_2O, in particular surface hydroxyls, in trapping holes at catalyst surfaces,[58, 61, 63-65] which is important for subsequent steps in the water oxidation reaction.

The CO_2 reduction reaction (CO_2RR) competes with the hydrogen evolution reaction (HER) in the presence of water and in general H_2O adsorption at catalyst surfaces is preferential to CO_2 adsorption.[66] It is therefore necessary to promote selectivity for the desired reactions. The adsorption of CO_2 molecules at titania surfaces has been studied using DFT and a crucial role has been ascribed to oxygen vacancies in the activation process.[67, 68] The presence of excess electrons and holes was shown to affect adsorption and activation of CO_2 at rutile (110), with implications for binding energies, structure and reactivity of adsorbed CO_2; both bent CO_2^- anion (excess electrons) and CO_2^+ cation (excess holes) configurations were identified with energy barriers of 1.12 eV and 0.75 eV respectively.[69] Yang and colleagues showed that sub-nm Pt clusters at the anatase (101) surface enhanced CO_2 activation through provision of additional adsorption sites at the edge of the Pt cluster, reporting increased adsorption strength and, in some instances, the spontaneous formation of a CO_2^- anion due to accumulation of negative charge on the C atom. The authors also reported transfer of electron density from the cluster to the TiO_2 substrate which facilitated adsorption at surface sites away from the supported Pt octamer.[70] Bismuth pyrochlore oxides have been shown to have a high CO_2 chemisorption capacity as identified through FTIR and attributed to the Bi_2O_3 motif with a Bi^{3+} lone pair.[71] Cu_2O has emerged as a potential candidate for CO_2RR due to its favourable band gap position and width[72] and studies have focussed on the interaction of CO_2 molecules with various cuprous oxide surfaces and terminations.[72-77] Wu and colleagues studied the adsorption of CO_2 at the Cu_2O (111): O terminated surface with oxygen vacancies,[75] finding that oxygen vacancies have a negative impact on the interaction energy; the most stable adsorption configuration at the perfect surface was more favourable by 0.15 eV than adsorption at the O vacancy surface. However, the authors also reported the formation of a stable $CO_2^{\delta-}$ radical anion species upon adsorption at the O vacancy surface, but this has an adsorption energy of ~0 eV. Another study examined the adsorption of CO_2 at Cu_2O (111) using Hybrid DFT[77] and

found adsorption only in non-activated form. Physisorption of a linear CO_2 molecule is favoured over adsorption in activated form at Cu_2O (111),[73, 76] however strong chemisorption, with energy gains of as much as 1.76 eV, was reported for CO_2 adsorption at the Cu-O terminated (110) surface.[73] Activation, with bending and elongation of bonds, upon exothermic (E_{ads} = -0.96 eV) adsorption of CO_2 at the (011) surface of CuO has been reported.[74] The conversion of CO_2 to methanol on Cu_2O nanolayers and clusters[72] was studied using Hybrid DFT with water as the source of H atoms for hydrogenation steps. Other theoretical studies have been conducted into reaction pathways involving the hydrogenation of CO and CO_2 at a variety of catalytic surfaces, including Cu/CeO_2 and $Cu/CeO_2/TiO_2$,[46] $Cu/ZnO/Al_2O_3$[78] and copper surfaces.[79, 80] Enhanced photoreduction of CO_2 with H_2O vapour has been reported for dispersed CeO_2 on anatase TiO_2, prepared using a one-pot hydrothermal method;[47] the role of Ce^{3+} in visible light absorption, photogenerated charge separation and strengthening CO_2-surface bonding was highlighted. The adsorption and activation of the CO_2 molecule at the catalyst surface is an important first step in subsequent reactions.

In the following we will present results of DFT studies of Ceria nanocluster modified rutile (110). Our clusters have compositions Ce_5O_{10} and Ce_6O_{12} and compliment earlier work on Ce_2O_3 reduced nanoclusters supported on rutile (110).[42, 48, 50] These nanoclusters allow us to examine composition effects on stability, band gaps, charge localization and reducibility. We show that adsorption of ceria-nanoclusters at the rutile (110) surface is favourable and that the nanocluster-surface composites favour non-stoichiometry so that reduced Ce ions will be present in the ground state. This off-stoichiometry leads to the emergence of Ce-derived occupied states in the band gap and low coordinated oxygen sites in the supported nanoclusters which contribute to the density of states (DOS) at the TiO_2-derived valence band maximum (VBM), potentially increasing the visible light response.

Results using a photoexcitation model show that the excited electron and hole prefer to localize onto the supported CeO_2 nanocluster. We will also present results which indicate that the interaction of CO_2 and H_2O is favourable at multiple sites of the reduced CeO_x-TiO_2 composite surfaces. CO_2 adsorbs and activates, forming a bent complex with elongated C-O distances. Finally, H_2O spontaneously dissociates at oxygen vacancy sites to generate surface bound hydroxyls.

2 METHODOLOGY

All calculations were performed using periodic plane wave density functional theory (DFT) as implemented in the VASP5.2 code.[81, 82] The valence electrons are described with a plane wave basis set with an energy cut-off of 396 eV. Projector augmented wave (PAW) potentials account for the core-valence electron interaction,[83, 84] with 4 valence electrons for Ti, 6 for O, 12 for Ce, 4 for C and 1 for H. The exchange-correlation functional is approximated by the Perdew-Wang (PW91) functional.[85]

Γ-point sampling is used for the (2×4) surface expansion of the rutile (110) surface with a supercell consisting of 18 monolayers (6 neutral trilayers) and a vacuum gap of 20 Å. The computed bulk lattice constants of rutile TiO_2 are $a = b = 4.64$ Å and $c = 2.97$ Å. The convergence criteria for the energy and forces are 10^{-4} eV and 10^{-2} eV Å^{-2} respectively. All calculations are spin polarized.

To consistently describe the partially filled Ti_{3d} and Ce_{4f} states a Hubbard U correction is applied.[86, 87] We use values of U(Ti) = 4.5 eV and U(Ce) = 5.0 eV with these values chosen from previous work on CeO_2 and TiO_2.[37, 38, 40, 48, 88, 89] For calculations involving the model excited state and valence band hole formation we apply an additional +U correction to the O_{2p} state with U(O) = 5.5 eV. Previous work has highlighted the necessity for such a correction in obtaining a correctly localized oxygen hole state in metal oxides.[33, 35-37, 40]

The ceria nanoclusters were adsorbed in different adsorption configurations at the rutile (110) surface which, for the purposes of this work, is free of the point defects and surface hydroxyls which can be present on real surfaces.[90, 91] The adsorption energies are computed using:

$$E_{ads} = E_{surf+A} - E_{surf} - E_A \quad (1)$$

where E_{surf+A}, E_{surf} and E_A are the energies of the adsorbate-surface composite system, the bare rutile (110) surface and the gas phase nanocluster respectively.

Once a stable adsorption configuration was identified we examined the energies associated with oxygen vacancy formation in the adsorbed CeO_2 nanocluster. One oxygen ion is removed from the adsorbed CeO_2 cluster and the vacancy formation energy is calculated as:

$$E_{vac} = E(Ce_xO_{y-1}) + 1/2E(O_2) - E(Ce_xO_y) \quad (2)$$

where the first and third terms on the right hand side of the equation are the total energy of the cluster-surface composite with and without an oxygen vacancy and the energy is referenced to half the total energy for molecular O_2. The calculation was performed for each oxygen site of the supported nanoclusters (see Table S1 *Supporting Information*) to determine the most stable non-stoichiometric composite. Once this is identified, we remove a second and third oxygen atom, as required, to describe situations in which multiple oxygen vacancies are present in the nanocluster (*vide infra)*. The oxidation states were determined through Bader charge analysis[92] and computed spin magnetizations and the corresponding values are quoted in the following sections.

We also investigated the adsorption and activation of H_2O and CO_2 at the CeO_2-modified rutile (110) composites, taking into particular account the presence of oxygen vacancies in CeO_2. The adsorption energies for the molecules adsorbed at the nanocluster are calculated as:

$$E_{int} = E_{surf+mol} - E_{surf} - E_{mol} \quad (3)$$

where $E_{surf+mol}$, E_{surf} and E_{mol} refer to the energies of the molecule and modified surface in interaction, the modified surface and the gas phase molecule (H_2O or CO_2) respectively.

We model photoexcitation by imposing a triplet electronic state on the system.[93] This promotes an electron to the conduction band, with a corresponding hole in the valence band, and enables an evaluation of the energetics and charge localization associated with photoexcitation. The following energies are computed:

- The ground state energy of the system, yielding $E^{singlet}$.
- A single point energy calculation at the ground state geometry with the triplet state imposed, yielding $E^{unrelaxed}$.
- An ionic relaxation of the triplet electronic state which gives $E^{relaxed}$.

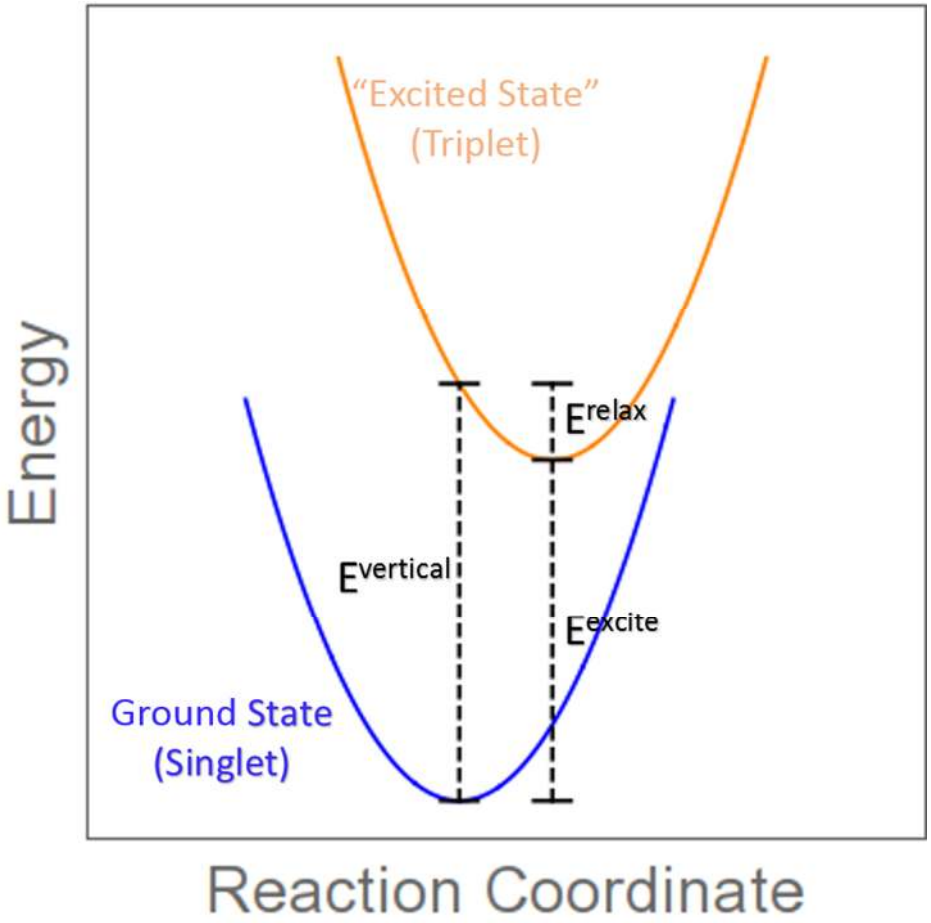

Figure 1. Schematic diagram of the relationship between the energies computed in the photoexcited model.

From the results of these calculations we compute:

1. The singlet-triplet vertical excitation energy:

$$E^{vertical} = E^{unrelaxed} - E^{singlet}.$$

This is the difference in energy between the ground (singlet) state and the imposed triplet state at the singlet geometry and corresponds to the simple VB-CB energy gap from the computed density of states.

2. The singlet-triplet excitation energy:

$$E^{excite} = E^{relaxed} - E^{singlet}.$$

This is the difference in energy between the relaxed triplet state and the relaxed singlet state and gives a crude approximation of the excitation energy.

3. The triplet relaxation (carrier trapping) energy:

$$E^{relax} = E^{unrelaxed} - E^{relaxed}.$$

This difference in energy between the unrelaxed and relaxed triplet states is the energy gained when the electron and hole are trapped at their metal and oxygen sites upon structural relaxation. This energy relates to the stability of the trapped electron and hole.

These quantities are summarized schematically in Figure 1.

3 RESULTS

3.1 Stoichiometric CeO_2-modified TiO_2 structures

We focus on ceria nanoclusters of two compositions, namely Ce_5O_{10} and Ce_6O_{12}, and we first examine the stoichiometric nanocluster adsorption energies and structures shown in Figures 2(a) and 2(d). The adsorption energies were computed using Eq. 1 and are -4.75 eV for Ce_5O_{10} and -2.47 eV for Ce_6O_{12} adsorption on rutile (110). The negative adsorption energies show that the interaction between the nanocluster and the surface is favourable, with the magnitude of the energy indicating the strength of the interaction. The larger adsorption energy for the Ce_5O_{10} nanocluster is reflected in the larger number of surface-to-nanocluster bonds; 7 compared with 6 for the adsorbed Ce_6O_{12} nanocluster. Another reason for the smaller adsorption energy of the Ce_6O_{12} cluster may be due to the presence of under-coordinated terminal oxygen ions and this idea will be expounded upon in the next section. From the

adsorption energies we expect the nanoclusters to be stable at the surface without desorbing or migrating over the surface to form aggregates. Henceforth, the composites will be denoted as Ce_5O_x-rutile-(110) and Ce_6O_x-rutile-(110), where the subscript x will vary according to the stoichiometry.

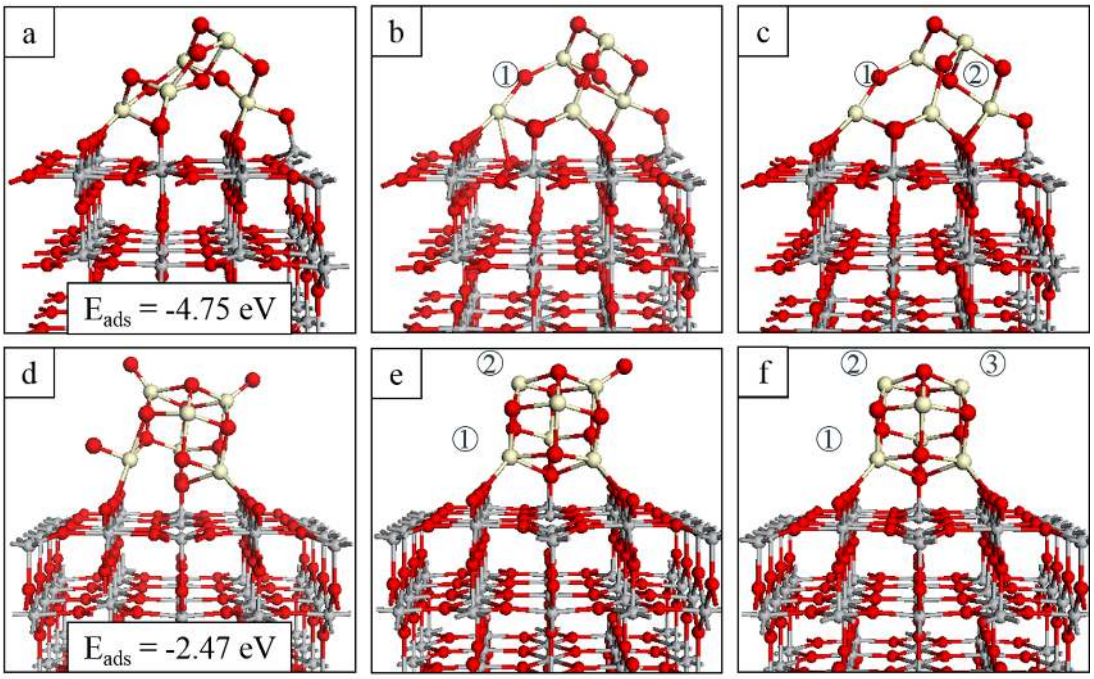

Figure 2. Top panels show the relaxed atomic structure of the Ce_5O_{10}-rutile (110) composite in **(a)** stoichiometric form and after the formation of **(b)** one (ground state) and **(c)** two (reduced state) oxygen vacancies. Bottom panels show the atomic structure of the Ce_6O_{12}-rutile (110) composite in **(d)** stoichiometric form and after the formation of **(e)** two (ground state) and **(f)** three (reduced state) oxygen vacancies. Insets of the left panels show the adsorption energies of the stoichiometric nanoclusters. The numbers in the black circles indicate the order in which oxygen atoms are removed from the nanocluster and are consistent with Table 1. In this and subsequent figures, Ti is indicated by a grey sphere, O by a red sphere and Ce by a cream sphere.

In the Ce_5O_{10}-rutile-(110) composite (Figure 2(a)), two of the cerium ions are coordinated to four cluster oxygen atoms, while three Ce cations are five-fold coordinated and form interfacial bonds with bridging oxygen ions of the surface with Ce-O distances of 2.3-2.4 Å. Each of the oxygen ions of the cluster are two-fold coordinated with the exception of one at the centre of the cluster which coordinates to three cluster cations. Three oxygens of the nanocluster bind to titanium ions in the surface with Ti-O distances of 1.8-2.0 Å.

For the Ce_6O_{12}-rutile-(110) composite (Figure 2(d)), five cerium cations are five-fold coordinated with one four-fold coordinated Ce cation. Two cations in the cluster each bind to two bridging oxygens of the surface with Ce-O distances of 2.4-2.6 Å. The cluster oxygens bind to three metal cations with the exception of three terminal oxygens which are singly coordinated to cerium ions. Ce-O distances involving singly coordinated O ions are 1.9 Å and compare with typical Ce-O distances in the range of 2.1-2.6 Å for the other O atoms in the cluster. Two cluster oxygens each form a single interfacial bond with surface titanium ions with Ti-O distances of 1.8 Å and 1.9 Å.

The interfacial bonding between the nanocluster and the surface results in an appreciable distortion of the local atomic structure at the surface. Where a bridging surface oxygen is bound to a nanocluster cation the Ti-O bond involving this oxygen elongated by up to 10% compared with a typical unmodified bond length of 1.88 Å. Surface titanium atoms that bind with oxygen in the nanoclusters migrate out of the surface plane towards the cluster by as much as 0.92 Å, lengthening the subsurface Ti-O distance.

3.2 Reduction of CeO_2-rutile by oxygen vacancy formation

From our relaxed stoichiometric nanocluster-surface composites we remove oxygen ions from CeO_2 and examine the energies involved in the formation of these vacancy sites. Previous work

on small CeO_2 structures on rutile (110) has shown that these prefer to be reduced, with loss of oxygen in the ground state, giving composition Ce_2O_3.[46, 48] It is not known if a similar composition would be found for larger but still sub-nm ceria clusters. The oxygen vacancy formation energies are important as their stability determines the stoichiometry of the composite. If the composite is then reduced, the formation energy can be a further important factor in determining if feedstock species will interact with the CeO_x-rutile composites. If the energy cost to form a reducing vacancy is low, the system favours non-stoichiometry and fixation and activation of molecular species, *via* a redox or Mars van Krevelen process, may not occur and no reactions can take place. On the other hand, while large vacancy formation energies can promote reoxidation *via* feedstock reduction, these require a large initial energy input and may also result in too strong interaction with molecular species, leading to poisoning of the surface.

Table 1 presents the computed oxygen vacancy formation energies in each supported ceria nanocluster. The most stable oxygen vacancy in Ce_5O_{10}-rutile-(110), which results in formation of Ce_5O_9-rutile-(110), has a small cost of 0.18 eV. A formation energy of this magnitude suggests that an off-stoichiometric ground state will be present. For a second oxygen vacancy, giving a composition Ce_5O_8-rutile-(110), the most stable vacancy site has an energy cost of 1.48 eV, relative to Ce_5O_9-rutile-(110). Thus the second oxygen vacancy is the reducing oxygen vacancy and this has a moderate cost.

For the Ce_6O_{12}-rutile composite, the first two oxygen vacancies have negative formation energies, of -0.46 eV and -0.16 eV, which means that the ground state is highly off-stoichiometric as the vacancies will form spontaneously at $T = 0$ K. The ground state therefore has the composition Ce_6O_{10}-rutile-(110). This instability of the stoichiometric Ce_6O_{12} nanocluster adsorbed on the rutile (110) surface sheds light on its small adsorption energy relative to the Ce_5O_{10} nanocluster. Computing the adsorption energy of an off-stoichiometric

Ce_6O_{10} nanocluster on rutile (110), yields a value of -3.45 eV, suggesting a stronger interaction at the surface and enhanced stability. The energy cost required to produce the third oxygen vacancy in the most stable cluster site of the larger nanocluster-surface composite is +0.30 eV. This is a moderate cost and we consider the Ce_6O_9-rutile-(110) composite as being in a reduced state. Thus, for the CeO_2-rutile composites, with rutile modified by a sub-nm ceria nanocluster, we expect a highly non-stoichiometric system with multiple potential activation sites at moderate temperatures, consistent with the work of Graciani *et al.*[46]

Table 1. Computed oxygen vacancy formation energies in CeO_2-rutile composites. The values listed correspond to the most stable configuration after removal of one, two or three oxygen atoms in the cluster and correspond to the numbering in Figure 2.

Reaction	**Oxygen vacancy**	**Formation energy (eV)**
$Ce_5O_{10} \rightarrow Ce_5O_9$	$E_{vac,1}$	+0.18
$Ce_5O_9 \rightarrow Ce_5O_8$	$E_{vac,2}$	+1.48
$Ce_6O_{12} \rightarrow Ce_6O_{11}$	$E_{vac,1}$	-0.46
$Ce_6O_{11} \rightarrow Ce_6O_{10}$	$E_{vac,2}$	-0.16
$Ce_6O_{10} \rightarrow Ce_6O_9$	$E_{vac,3}$	+0.30

Figure 2 shows the atomic structures of the non-stoichiometric ground state (2(b) and 2(e)) and reduced (2(c) and 2(f)) nanocluster-surface composites; the black circles in the images indicate the site number of the removed oxygen, corresponding to Table 1.

After formation of the first oxygen vacancy in Ce_5O_{10}-rutile-(110), the two Ce ions which were bonded to this oxygen maintain their coordination by forming new interfacial bonds to oxygen atoms in the rutile (110) surface (Figure 2(b)). In total, three new nanocluster-surface bonds

are formed, two involving bridging oxygen and the third involving an in-plane surface oxygen which migrates out from the surface by 0.1 Å. One Ce-O bond is broken during the relaxation; the coordination of the Ce is maintained by binding to the central O atom of the nanocluster with the latter now four-fold coordinated. After formation of the second vacancy, yielding Ce_5O_8-rutile-(110) (Figure 2(c)), one of the Ce ions is three-fold coordinated, while the remaining cerium are four- and five-fold coordinated. In both the off-stoichiometric ground state, with one O vacancy, and the reduced composite, with two O vacancies, there are nine interfacial bonds, up from seven in the stoichiometric Ce_5O_{10}-rutile composite.

For the Ce_6O_{12}-rutile-(110) composite, the formation of oxygen vacancies to produce the ground state, Ce_6O_{10}-rutile-(110) (Figure 2(e)), and reduced, Ce_6O_9-rutile-(110) (Figure 2(f)), composites has no impact on the number of interfacial bonds. However, the Ce ions to which the removed terminal O atoms were bound, relax towards the nanocluster, increasing their coordination by binding to O atoms of the nanocluster.

In these non-stoichiometric nanocluster-surface composites we expect to find two electrons released for each neutral oxygen vacancy and the spin density plots are used to determine the location of the electrons after relaxation. The spin density plots for the ground and reduced states of CeO_x-rutile are presented in Figure 3 and show that electron localization occurs at Ce atoms in each nanocluster, which results in the formation of reduced Ce^{3+} cations. Ce^{3+} form in preference to Ti^{3+} cations and this has also been seen in DFT+U studies of Ce-doped TiO_2[94-96] and some surfaces.[42, 50]

For the non-stoichiometric ground state structures, the smaller nanocluster has a Ce_5O_9 configuration and two Ce atoms are reduced as shown in Figure 3(a). For the larger nanocluster the ground state has a Ce_6O_{10} composition and four reduced Ce atoms are shown in Figure 3(c). When the composites are reduced, giving compositions Ce_5O_8-rutile-(110) and Ce_6O_9-rutile-

(110), four Ce atoms are reduced in the smaller nanocluster (Figure 3(b)), and all six Ce atoms are reduced in the larger cluster (Figure 3(d)).

These results are further confirmed through Bader charge analysis, the results of which are included in Table 2. Typical net atomic charge values for Ce^{4+} ions are in the range of 9.6 to 9.8 electrons for the stoichiometric nanoclusters. Upon oxygen vacancy formation and the subsequent localization of excess spin on Ce atoms to give a +3 oxidation state, the net atomic charges increase by 0.2 electrons for affected cations; this is typical for $Ce^{4+} \rightarrow Ce^{3+}$ reduction. The computed spin magnetizations for reduced Ce^{3+} cations are 0.97-0.98 $_B$.

In general, Ce-O distances involving Ce^{3+} species are elongated by 0.1-0.2 Å due to the larger ionic radius of Ce^{3+} compared to Ce^{4+}; this effect is less strong in cases where the reduced Ce ions have a lower coordination or where the Ce ion was previously bound to a singly coordinated O atom. See Table S2 in the *Supporting Information* for details of the Ce-O distances in each case.

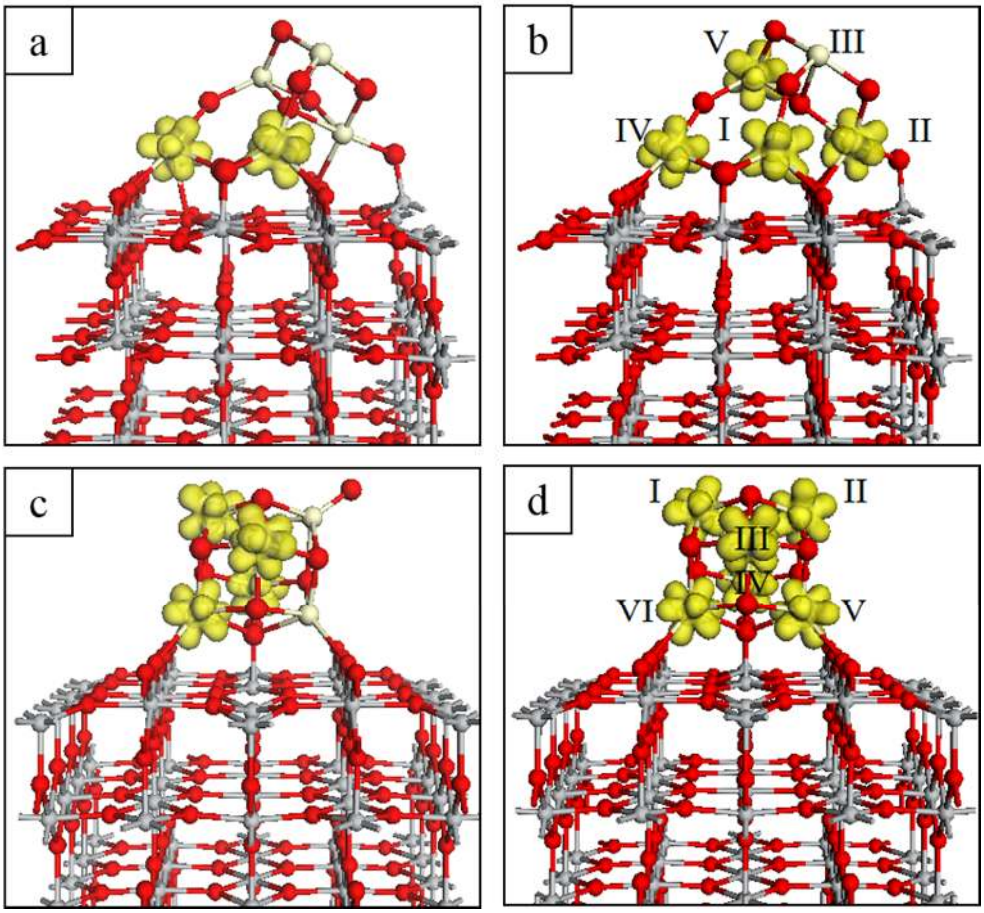

Figure 3. Excess spin density plots for Ce_5O_{10}-modified rutile (110) surface with **(a)** one (ground state) and **(b)** two (reduced) oxygen vacancies and Ce_6O_{12}-modified rutile (110) surface with **(c)** two (ground state) and **(d)** three (reduced) oxygen vacancies. The spin density isosurfaces are yellow and enclose spin densities of up to 0.2 eV/Å^3. The roman numerals in the panels on the right hand side correspond with the labelling in Table 2.

Table 2. Computed Bader charges for the cerium ions in the supported nanoclusters before and after formation of one or more oxygen vacancies. Superscripts [a], [b], and [c] denote the

stoichiometric, off-stoichiometric ground state, and reduced nanocluster-surface composites respectively. Reduced Ce^{3+} are highlighted in bold.

	[a]Ce_5O_{10}	[b]Ce_5O_9	[c]Ce_5O_8		[a]Ce_6O_{12}	[b]Ce_6O_{10}	[c]Ce_6O_9
Ce_I	9.6	**9.9**	**9.9**	Ce_I	9.7	**10.0**	**10.0**
Ce_{II}	9.6	9.6	**9.9**	Ce_{II}	9.7	9.8	**10.0**
Ce_{III}	9.8	9.8	9.8	Ce_{III}	9.8	**10.0**	**10.0**
Ce_{IV}	9.7	**9.9**	**9.9**	Ce_{IV}	9.7	**9.9**	**9.9**
Ce_V	9.7	9.7	**10.0**	Ce_V	9.7	9.7	**9.9**
				Ce_{VI}	9.7	**9.9**	**9.9**

The spin polarized projected electronic density of states (PEDOS) for the stoichiometric, off-stoichiometric ground state and reduced nanocluster-surface composites described above are presented in Figure 4. Panels (a) and (d) of Figure 4 show the stoichiometric configurations where the most obvious feature is the presence of states due to cluster oxygens at the top of the valence band for the Ce_6O_{12} nanocluster. These states are due to the singly coordinated oxygen ions described previously. However, the nanocluster-derived oxygen 2p states above the TiO_2 VB persist even after removing these oxygen sites. In panels (b), (c), (e) and (f), which correspond to the off-stoichiometric CeO_x-rutile composites, we can see that the presence of reduced Ce^{3+} cations in the nanoclusters after formation of oxygen vacancies introduces states into the TiO_2-derived band gap. These states arise due to the singly occupied $4f^1$ orbital configuration of the reduced Ce^{3+} cations. The modification of rutile with CeO_x nanoclusters will result in a red shift of the TiO_2 adsorption edge; this is due to a combination of 2p states

of low coordinated O sites of the cluster pushing the VBM to higher energy and the emergence of mid-gap states associated with reduced Ce^{3+} ions in the off-stoichiometric composites.

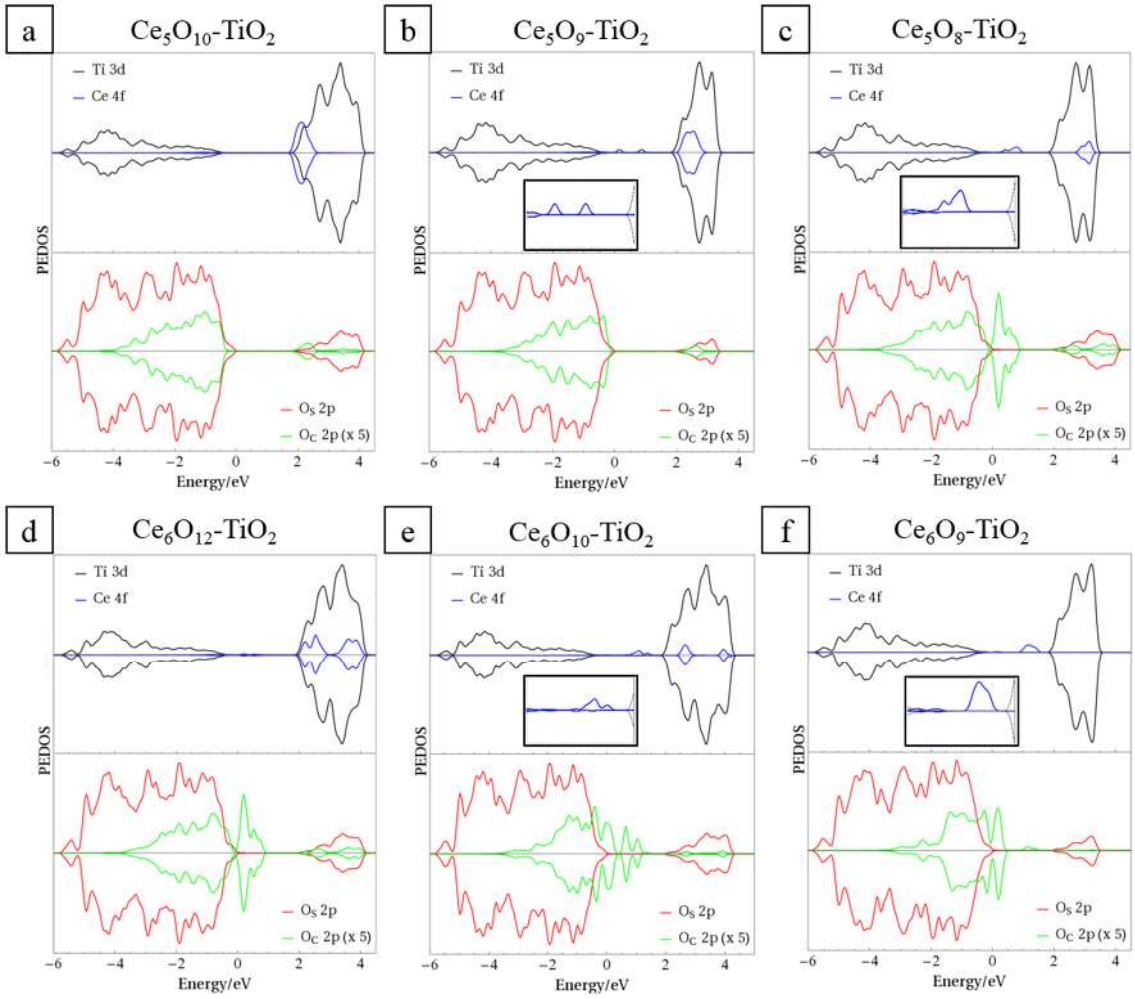

Figure 4. Spin polarized projected electron density of states (PEDOS) for **(a)** Ce_5O_{10}-, **(b)** Ce_5O_9-, **(c)** Ce_5O_8-, **(d)** Ce_6O_{12}-, **(e)** Ce_6O_{10}- and **(f)** Ce_6O_9-rutile-(110). The top half of each panel displays Ti 3d- and Ce 4f-derived states. Bottom halves of the panels display contributions to the DOS from surface (O_S) and nanocluster (O_C) oxygen 2p-derived states. Insets in the top panels show the mid-gap Ce-derived states in the range -0.5 eV – 2.0 eV.

3.3.3 Modelling charge separation upon photoexcitation.

We apply the photoexcited model to the ground state CeO_x-TiO_2 systems which consist of the off-stoichiometric composites, Ce_5O_9-rutile-(110) and Ce_6O_{10}-rutile-(110). Table 3 presents the computed vertical and singlet triplet energies and the electron-hole localization (relaxation) energies, as discussed in Section 2. Firstly, we note the underestimation of the bandgap inherent in approximate DFT is present in our DFT+U computational set-up. The +U corrections used herein are chosen to consistently describe the localization of electrons and holes rather than to reproduce the bandgap of bulk TiO_2, which is not advised. This underestimation is clear in the computed values for $E^{vertical}$ and E^{excite} which are clearly smaller than the experimental values. However, what is important for our study is the change in these quantities with modification of the rutile (110) surface.

Table 3. Vertical singlet-triplet energy difference ($E^{vertical}$), the relaxed singlet-triplet energy difference (E^{excite}) and the relaxation energy (E^{relax}) for nanocluster rutile (110). Values for unmodified rutile (110) have been included for reference.

Composite structure	**$E^{vertical}$ (eV)**	**E^{excite} (eV)**	**E^{relax} (eV)**
Bare-rutile (110)	2.02	1.97	0.05
Ce_5O_9-rutile (110)	1.76	0.96	0.80
Ce_6O_{10}-rutile (110)	1.30	0.51	0.80

We note that E^{excite} is always smaller than $E^{vertical}$ and the simple valence-conduction band energy difference, as the former energy includes the ionic relaxations and polaron formation in response to "exciting" the electron which then lowers the energy of the triplet electronic state. Comparison of these computed energies across different structures yields useful qualitative information about the effect of surface modification. In particular, a reduction in E^{excite} for a

composite structure relative to the unmodified metal oxide will correspond to a red shift in light absorption for the surface modified system. The energies presented in Table 3 show that modification of the (110) surface of rutile TiO_2 with nanoclusters of CeO_2 leads to a red shift in light absorption whether we use the vertical or excitation energies. This effect is stronger for the larger nanocluster, consistent with the PEDOS. Relaxation energies of 0.8 eV upon charge localization in each heterostructure indicate high stability of the photogenerated electron-hole pairs.

We can also examine the localization of the electron-hole pair through analysis of computed Bader charges, spin magnetizations and excess spin density plots. Figure 5 shows the spin density plots for Ce_5O_9- and Ce_6O_{10}-rutile-(110) after relaxation of the triplet state; electrons are shown in yellow and holes are represented in blue. Since both modifiers are off-stoichiometric in the ground state, reduced Ce^{3+} ions are already present prior to imposing the excited state. For the Ce_5O_9-rutile-(110) system, shown in Figure 5(a), there are three unpaired electrons; two are due to the neutral oxygen vacancy and are localized at Ce_I and Ce_{IV} (compare with Figure 3(a)). The third electron is the photoexcited electron and is localized on Ce_{II}; this Ce ion, which was five-fold coordinated in the ground state, is four-fold coordinated after localization of the photoexcited electron and the Ce-O bonds are elongated by as much as 10%. For the Ce_6O_{10}-rutile-(110) composite, shown in Figure 5(b), there are five unpaired electrons; four are due to the formation of two neutral oxygen vacancies and are localized at Ce_I, Ce_{III}, Ce_{IV} and Ce_V (compare with Figure 3(c)). The fifth photoexcited electron localizes at Ce_V; Ce_V maintains a six-fold coordination, and the Ce-O distances increase by up to 10% relative to their values in the ground state. In all instances electron localization at Ce ions in the nanocluster increases the computed Bader charges by 0.2 electrons, similar to the trend presented in Table 2, and spin magnetizations of 0.97 $_B$ were computed for these sites.

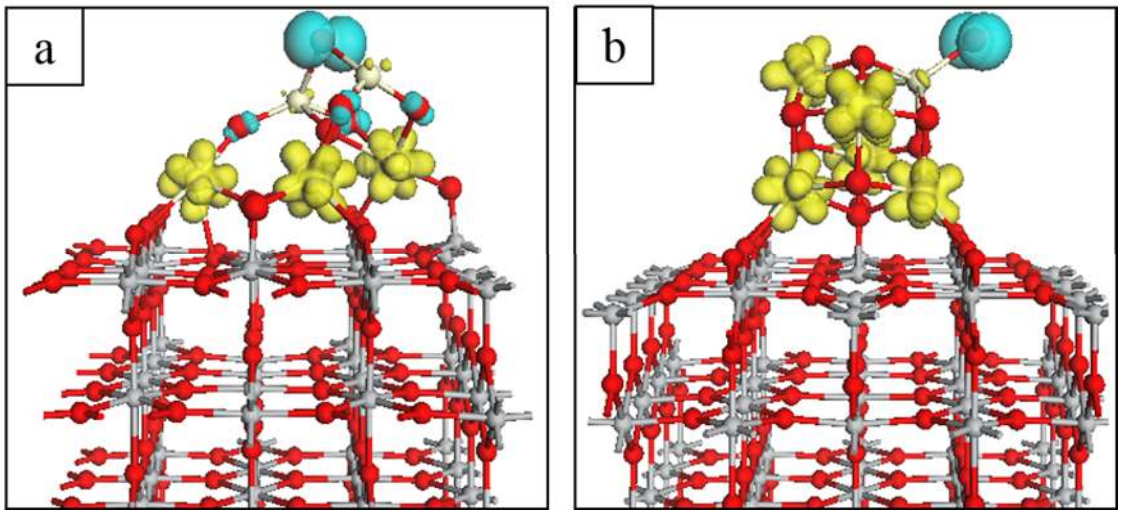

Figure 5. Spin density plots for the photoexcited electron and hole in **(a)** Ce_5O_9-rutile-(110) and **(b)** Ce_6O_{10}-rutile-(110). The spin density isosurfaces are yellow for electrons and blue for holes and enclose spin densities of up to 0.02 eV/Å^3.

For both modified surfaces we see that the hole predominantly localizes on a single, low-coordinated oxygen site of the nanocluster, shown in blue in Figure 5. For the Ce_5O_9-rutile-(110) composite (Figure 5(a)) the oxygen site at which the hole predominantly localizes is two-fold coordinated both before and after photoexcitation; the Ce-O distances increase from 2.1 Å in the ground state to 2.4 Å in the excited state. In the Ce_6O_{10}-rutile-(110) system (Figure 5(b)) the hole localizes at a singly coordinated terminal oxygen site; the Ce-O distance increases from 1.9 Å in the ground state to 2.3 Å after excitation. Hole localization is accompanied by a change in the computed Bader charge of the oxygen by 0.4 electrons, from 7.1 to 6.7 electrons, in each case. For the Ce_5O_9-rutile-(110) composite there is some spreading of the hole to neighbouring two-fold coordinated oxygen sites of the nanocluster but this spreading is typical for this DFT+U set-up and is accompanied by changes of < 0.1 electrons in the computed Bader charges, so that we can conclude the hole predominantly localizes on one oxygen site in the

nanocluster. This is confirmed by a computed spin magnetization of 0.73 $_B$ for the oxygen hole on Ce_5O_9-rutile-(110) and compares with a value of 0.78 $_B$ for the singly terminated oxygen site at which the hole localizes in Ce_6O_{10}-rutile-(110).

For the CeO_x-rutile-(110) composites we can see that both the electron and hole localize on the nanocluster modifiers, which may have consequences for recombination. However, in looking at Figure 5 we see that the spatial separation of the charges is maximal, given that both electrons and holes localize at nanocluster sites. In addition, the large relaxation or trapping energies act to impede migration of the charges and thus the impact on recombination should be minor. We also note that our photoexcited model, which involves the imposition of a triplet state to induce a transition from the VB to the CB, precludes transitions from the highest occupied, Ce 4f-derived states of the off-stoichiometric ground states (see Figures 4(b) and 4(e)). Such transitions would amount to electron hopping between Ce sites of the nanocluster with no change in electronic configuration after "excitation". Rather, our model with a triplet electronic state (in addition to the unpaired electrons on reduced Ce^{3+}) will induce transitions from O_C 2p-derived states, which sit at the top of the titania-derived VB, to the unoccupied Ce 4f states.

3.4 CO_2 adsorption at the reduced nanocluster-surface composites.

With the motivation that O vacancies in reduced metal oxides can act as sites for the adsorption and activation of CO_2, as found in other studies,[75, 97-100] we have examined the adsorption of CO_2 at various sites on our reduced Ce_5O_8- and Ce_6O_9-rutile-(110)); the computed adsorption energies for the most stable configurations are -1.36 eV on Ce_5O_8-rutile-(110) and -1.09 eV on Ce_6O_9-rutile-(110). The relaxed geometries for these configurations are shown in Figure 6. The *Supporting Information* shows additional adsorption structures and energies for the CO_2-CeO_x-TiO_2 interaction.

The most stable CO_2 adsorption sites have negative adsorption energies and the magnitudes of these adsorption energies are indicative of a strong exothermic interaction between CO_2 and the oxides. Our results follow the trend that CO_2 interaction is stronger at vacancy sites with a higher formation energy, as previously reported.[31] A DFT+U study of CO_2 activation on CeO_2 (110) found that the most stable O vacancy had a formation energy of +1.65 eV;[101] the authors reported that CO_2 adsorption at this site, with a bent geometry and E_{ads} = -1.22 eV, was the most stable adsorption configuration. A DFT+U study of CO_2 reduction on CeO_2 (111) also found that interaction was strongest at the O-defective surface;[102] the O vacancy formation energy was +2.78 eV and CO_2 adsorbed in a bent geometry with E_{ads} = -1.12 eV. While the adsorption energies are comparable across these studies, the vacancy formation energy is not sufficient in predicting the strength of interaction of adsorbed CO_2. Previous work on Ce_3O_6-rutile-(110)[31] found that this composite was reducible with an O vacancy formation energy of +0.31 eV; CO_2 was calculated to adsorb exothermically with E_{ads} = -0.20 eV. This compares with an adsorption energy of -1.09 eV for CO_2 interacting at the reduced Ce_6O_9-rutile-(110) composite of the present work in which oxygen vacancies are produced with similar energy costs (see Table 1). This would suggest that, in the case of ceria nanocluster modifiers, the degree of non-stoichiometry, which is related to the number of reduced Ce cations in the cluster, may play a role in stabilizing adsorbed surface species. Future work, involving larger ceria nanocluster modifiers, can shed further light on the nature of the trade-off between interaction strength and reducibility.

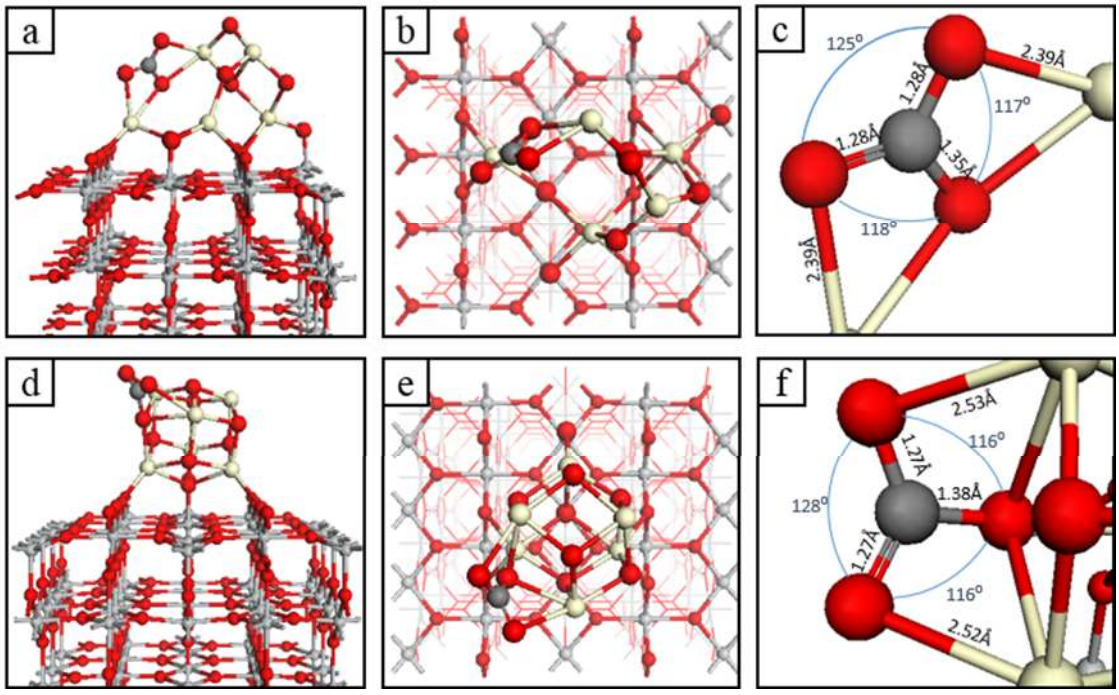

Figure 6. Relaxed atomic structure for most stable configurations of CO_2 adsorbed at **(a)**, **(b)** and **(c)** Ce_5O_8-rutile-(110) and **(d)**, **(e)** and **(f)** Ce_6O_9-rutile-(110). **(a)**, **(d)** Side views; **(b), (e)** top views and **(c), (f)** key geometry data around the CO_2 adsorption site. Carbon atoms are indicated by dark grey spheres.

The relaxed structures of the most stable configurations of CO_2 adsorbed at the CeO_x-TiO_2 heterostructures are similar across both nanocluster modifiers and all sites. Adsorption tends to favour the formation of an activated CO_2 complex which has two elongated C-O bonds in the adsorbed CO_2 molecule and a third, longer C-O bond involving an oxygen from the nanocluster near the adsorption site. This results in a surface bound species with the binding further strengthened by the interaction of the oxygen atoms of CO_2 and Ce cations in the nanoclusters.

The O-C-O angle of the adsorbed CO_2 molecule is in the range of 125-128^0 depending on the adsorption site, while the two O-C-O angles involving the cluster oxygen are in the range of

115-118^0. This deviation of the O-C-O angle from 180^o in the linear gas phase CO_2 is a key signature of CO_2 activation, as discussed on other systems.[103-105] C-O bonds in CO_2 have distances between 1.26 and 1.28 Å with the remaining (cluster oxygen) C-O bond length in the range of 1.35-1.39 Å. Thus, the C-O bonds in adsorbed CO_2 are significantly elongated over the gas phase (C-O ≈ 1.16 Å) coupled with considerable bending of the O-C-O bond angle. This means that the interaction leads to an activated, chemisorbed CO_2 species and the formation of a carbonate species can be ruled out.

The Ce-O bonds established with the adsorbed species are comparable in length to those within the nanocluster which are typically in the range of 2.2-2.6 Å. The calculated Bader charges show that charge transfer is qualitatively consistent across the various adsorption sites. Between 0.1 and 0.2 electrons are transferred from the CO_2-derived O atoms to the cluster while the cluster oxygen site with which the CO_2 interacts gains between 0.4 and 0.6 electrons through the interaction.

3.5 H_2O adsorption at the reduced nanocluster surface composites.

We also examined how water interacts at the vacancy sites in the reduced CeO_x-rutile (110) composites. We compute the adsorption energies of H_2O interacting at a range of sites of the reduced Ce_5O_8- and Ce_6O_9-rutile-(110) surfaces using Eq. 2. We find that adsorption of water is favourable at multiple sites on the CeO_x nanocluster. Adsorption energies for the most stable adsorption configurations of water are -1.8 eV on Ce_5O_8-rutile-(110) and -0.9 eV on Ce_6O_9-rutile-(110); the corresponding geometries displayed in Figure 7. The *Supporting Information* shows additional adsorption sites and energies for the H_2O-CeO_x-TiO_2 interaction.

In the interaction of H_2O at the reduced composites, starting from an initial water adsorption in molecular form, the most stable adsorption mode is that in which the water molecule

dissociates spontaneously upon relaxation. This dissociation involves the transfer of an H atom to an O site of the supported nanocluster and the hydroxyl from the water molecule bridges two cluster Ce sites. On the larger CeO_x nanocluster, the moderate adsorption energy means that hydroxyls should not be overstabilized and could be active in catalysis. Thus, water dissociation and activation can be promoted on these ceria-rutile composites.

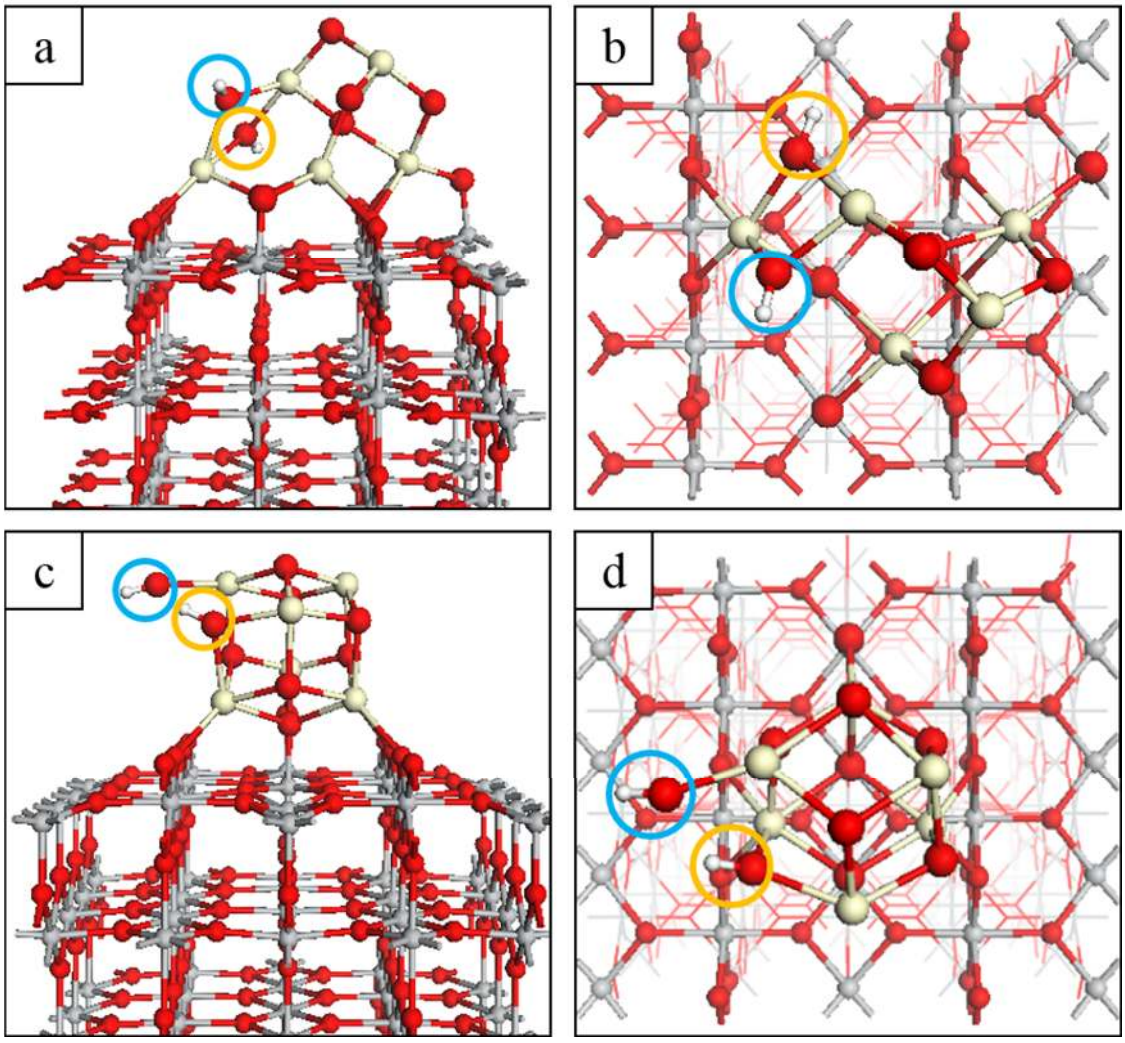

Figure 7. Relaxed atomic structures of the most stable configurations of H_2O adsorbed at **(a)** and **(b)** Ce_5O_8-rutile-(110) and **(c)** and **(d)** Ce_6O_9-rutile-(110). Hydroxyl groups arising from the spontaneous dissociation at the surface are circled in blue for the water-derived OH and in orange for the OH involving a cluster O site. H atoms are represented by small white spheres.

For adsorption of water at the Ce_5O_8 nanocluster (Figures 7(a) and 7(b)), the water molecule interacts with low-coordinated cluster sites. The OH group fills a vacancy site (O_1 from Figure 2(b)), and binds to two Ce^{3+} sites which were four- and three-fold coordinated; the latter being the lowest coordinated cluster cation. The second H atom transfers to a two-fold coordinated cluster O site which neighbours the Ce sites bound to the hydroxyl and is among the lowest-coordinated cluster anion sites. Ce-O bond lengths involving both cluster- and water-derived OH groups are elongated by as much as 0.3 Å relative to equivalent Ce-O distances prior to water adsorption. Bader charge analysis reveals that there is no charge transfer between the nanocluster and water and no Ce^{3+} cations are reoxidized. There is a charge redistribution, with an increase in charge of 0.3 electrons in the nanocluster as a result of formation of hydroxyls, which is predominantly transferred to oxygen in the nanocluster that binds with hydrogen.

For the reduced Ce_6O_9 nanocluster, the O sites (Ce sites) show three-fold (four-fold) or higher coordination. The water molecule dissociates upon adsorption with transfer of an H atom to a cluster O site and the OH group binding to a single neighbouring Ce ion (Figures 7(c) and 7(d)). The cluster anion and cation adsorption sites remain three- and four-fold coordinated after the interaction due to the breaking of their mutual bond. Ce-O bond lengths involving the cluster-derived OH group are elongated by 0.15 Å relative to their values before water adsorption. The distances between the Ce atom at which the water-derived OH group is adsorbed and the nanocluster O atoms with which it still shares bonds are similarly elongated. Despite this distortion of the larger nanocluster upon H_2O adsorption, the interaction is strong and favourable as shown by an adsorption energy of -0.9 eV. Similarly to the smaller nanocluster, there is a redistribution of charge with water oxygen transferring 0.3 electrons to the nanocluster and this charge is donated to the nanocluster oxygen that binds with hydrogen from water.

These results compare with studies of water dissociation at Ce_2O_3-TiO_2.[48, 106] In these studies the authors followed the energy pathway from water adsorbed in molecular form to dissociation, finding that the dissociation process was exothermic (-0.70 eV) with a small energy barrier of 0.04 eV. We found that dissociation of molecular water occurred spontaneously, suggesting that the size of the supported CeO_x nanocluster and the number of Ce^{3+} sites play a role in the ability of the composite to dissociate water.

While the ability of metal oxides to dissociate H_2O is well established, the mechanism which promotes dissociation upon adsorption remains of interest. A number of studies have looked at CeO_2 surfaces as model systems for the study of water dissociation.[107-110] Defects, step edges and terraces in surfaces play a role as such features provide low-coordinated adsorption sites. CeO_2 (111) with O vacancies and Ce^{3+} ions shows a preference for dissociative water adsorption, relative to the pristine surface, where there is little energetic difference between adsorption in molecular and dissociated form.[111] Similar results were found by Carrasco and colleagues for CeO_2 (111);[112] the presence of O vacancies made dissociative adsorption more favourable, by 1.1 eV relative to molecular water, with no energy barrier. The authors also found that Ni and Ni_4 at the surface introduced Ce^{3+} ions and had a moderating effect on the water adsorption energies; for Ni/CeO_2(111), dissociation was favoured by 0.3 eV with a small energy barrier of 0.13 eV. High lying 2p states, derived from low coordinated O sites in the nanocluster, with the presence of Ce^{3+} states in the gap facilitates interactions with water to break O-H bonds. A recent study has shown that increased lattice strain in the CeO_2 (111) surface promotes dissociation of H_2O over molecular adsorption.[113] For the reduced Ce_6O_9-rutile-(110) composite, the Ce-O distances, at the sites of H_2O adsorption (see Figures 7(c) and (d)), are longer by ~1% relative to typical distances (~2.37 Å) in the pristine CeO_2 (111) surface. This suggests that tensile strain may indeed contribute to promoting the dissociation of water. In Ce_5O_8-rutile-(110), Ce-O distances are shorter (~2.2 Å), due to the lower

coordination of the cluster O sites, and elongate after the dissociative adsorption of H_2O. However, the Ce-Ce distance prior to water adsorption is 4.2 Å, which is considerably longer than neighbouring Ce-Ce distances (~3.9 Å) in CeO_2 (111). After the dissociative adsorption of water, this Ce-Ce distance decreases to 3.6 Å, further indicating that tensile strain may play a role in driving the dissociation.

Figure 8 shows the PEDOS of the H_2O molecule and reduced CeO_x-rutile-(110) composites in the non-interacting case (H_2O + surface) and after dissociative adsorption (H_2O-surface). For the non-interacting systems the molecule and surface are relaxed in the same unit cell with sufficient spatial separation such that they do not interact. In the non-interacting cases (left panels of Figure 8), the water-derived O_W 2p states are well defined peaks at energies of -2.9 eV and -0.8 eV (Figure 8(a)); -3.9 eV and -2.0 eV (Figure 8(c)) relative to the VBM (0 eV) of the TiO_2 support. For the interacting cases (right panels of Figure 8) the O_W 2p-derived states overlap the O_C 2p-derived states near the VBM of the titania host. The differences in the adsorption geometries, and perhaps the underlying mechanisms driving dissociation, are reflected in the behaviour of the O_W 2p-derived states after adsorption. For dissociated water on the Ce_6O_9-rutile-(110) surface, a sharp O_W 2p-derived peak lies above the VBM because the OH group is terminal, coordinating to a single Ce site. For adsorption at the Ce_5O_8-rutile-(110) composite, the O_W 2p states broaden and lie below the VBM, overlapping with O_C derived states, as in this instance the OH groups each bridge two Ce sites of the nanocluster. Comparing Figures 8(a) and 8(b), the O_W-derived states are shifted to lower energies upon dissociative adsorption. This trend is not seen in comparing Figures 8(c) and 8(d) due to the aforementioned singly coordinated OH group which results from adsorption of H_2O at the Ce_6O_9-rutile-(110) surface.

Despite these differences, some trends are consistent across both composites. In both cases the interaction increases the gap between the occupied Ce 4f-derived states and the CBM of the

TiO_2 host (see insets of panels in Figure 8); i.e. the occupied Ce^{3+} states are pushed to lower energy after interaction. In addition, integrating the O_C and O_W-derived DOS lying above the TiO_2 VBM in both the non-interacting and interacting cases shows that after interaction the occupied states are driven to lower energies. For both composites the number of states lying above the TiO_2 VBM is reduced by 2 in the interacting cases relative to the non-interacting systems; this suggests that passivation of high lying O 2p states is a factor driving the interaction of water with the reduced CeO_x-rutile-(110) composite surfaces.

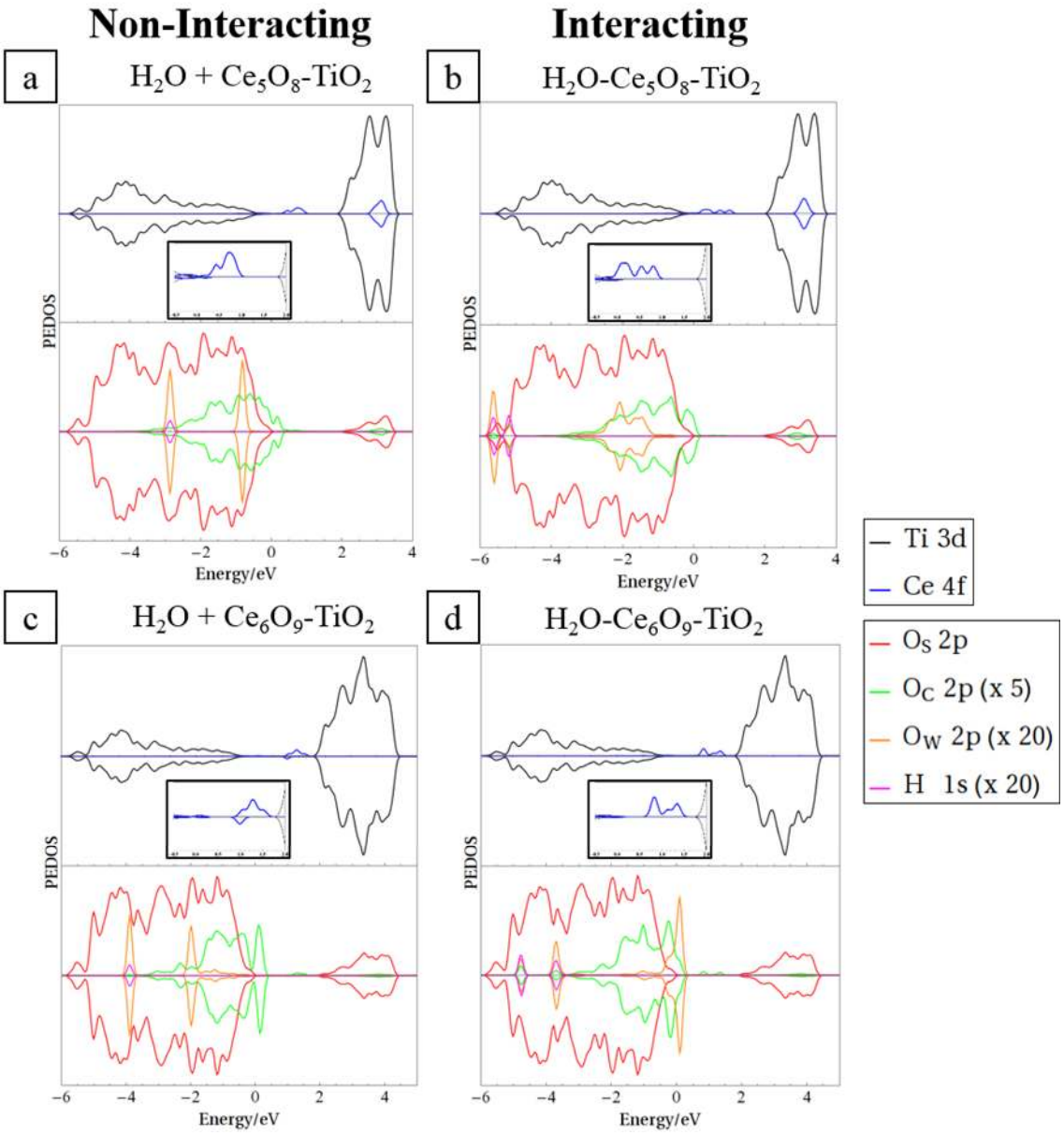

Figure 8. Spin polarized projected electron density of states (PEDOS) for **(a)** H_2O + Ce_5O_8-rutile-(110) (non-interacting), **(b)** H_2O-Ce_5O_8-rutile-(110) (interacting), **(c)** H_2O + Ce_6O_9-rutile-(110) (non-interacting) and **(d)** H_2O-Ce_6O_9-rutile-(110) (interacting). The top half of each panel displays Ti 3d- and Ce 4f-derived states. Bottom halves of the panels display contributions to the DOS from surface (O_S), nanocluster (O_C) and water (O_W) oxygen 2p-derived states and H 1s states. Insets in the top panels show the mid-gap Ce-derived states in the range -0.5 eV – 2.0 eV.

3.4 CONCLUSIONS

We have studied the (110) surface of rutile TiO_2 modified with ceria nanoclusters of compositions Ce_5O_{10} and Ce_6O_{12} using first principles DFT+U analysis. Our results show that the ground state of the nanocluster-surface composites is off-stoichiometric with one or more oxygen vacancies forming spontaneously or at very low energy cost, so that under typical experimental conditions, there will be oxygen vacancies present. The consequence of this is that Ce^{3+} ions will be present in the nanoclusters in their ground state (with no Ti^{3+} species) and this leads to the emergence of occupied Ce 4f-derived states in the TiO_2-derived bandgap. Together with CeO_x-derived O 2p states above the TiO_2 VB, this may induce a red shift in light absorption making these systems visible light active. It is low-coordinated oxygen atoms in the supported nanoclusters that contribute to these new states above the valence band edge.

In our model of the photoexcited state, in which an electron is promoted from the O 2p derived valence band, we found that electron and hole localization occur at Ce and low-coordinated oxygen sites on the supported nanocluster respectively. The consequence of this for charge recombination may not be detrimental as the electron-hole pair has a large trapping energy of 0.8 eV so this can reduce the migration of charges over the nanocluster. Verification of both the predicted red shift and the charge recombination effects would be welcome.

In terms of activity, the CeO_2-rutile composites are more reducible compared to the unmodified rutile (110) surface and moderate energy inputs are required to produce multiple oxygen vacancies. Electrons released after forming the oxygen vacancies localize on Ce sites in the supported nanoclusters. We have examined the interaction of oxygen vacancies in the reduced composites with CO_2 and H_2O to determine how CeO_x-rutile-(110) activates these molecules. We find that CO_2 adsorption is favourable at multiple sites on the nanocluster-modified surface,

with exothermic adsorption energies up to 1.36 eV. This strong adsorption is accompanied by a distortion from the linear gas phase CO_2 geometry, in which the molecule bends, with O-C-O angles of 125°-128°, and the C-O bonds in CO_2 show an elongation of ~0.10 Å. In combination with some transfer of charge between the adsorbed species and the nanocluster, this suggests the formation of activated CO_2 which is the crucial first step in the transformation of CO_2 to more useful molecules. We welcome attempts to study these materials for their ability to activate and convert CO_2, although the actual conversion process may be limited by other factors. Nevertheless, the finding that these ceria-modified TiO_2 systems can activate CO_2 is a promising first step.

Finally, the interaction of H_2O at the ceria-modified rutile composites was investigated. This is important for a number of reactions, such as water gas shift or water oxidation and one of the limiting steps in these reactions is water dissociation which usually has an energy cost and an activation barrier. On both reduced ceria-TiO_2 systems, water adsorption is exothermic and favourable and, importantly, this leads to spontaneous dissociation of water to form surface bound hydroxyls.

The results of this paper show that ceria-modified rutile TiO_2 composites can (1) have reduced Ce^{3+} cations, (2) show red shift in light absorption, (3) adsorb and activate carbon dioxide and (4) adsorb and activate water. This makes these composites interesting materials for the activation and conversion of CO_2 and water.

ACKNOWLEDGEMENTS

Financial Support from Science Foundation Ireland through the Starting Investigator Research Grant Project EMOIN SFI/SIRG/09/I2160, the Science Foundation Ireland US-Ireland R&D Partnership Program Project SusChem SFI/US/14/E2915 and the ERA.Net for Materials

Research and Innovation (M-ERA.Net 2), Horizon 2020 grant agreement number 685451, Science Foundation Ireland, Ireland, Grant Number SFI/16/M-ERA/3418 RATOCAT is gratefully acknowledged. Access to the computational resources at the Science Foundation Ireland/Higher Education Authority funded Irish Center for High End Computing is acknowledged. We are grateful for support from the COST Action CM1104 "Reducible Metal Oxides, Structure and Function" We acknowledge important discussions with Profs. K. A. Gray, E. Weitz and J. A. Byrne.

REFERENCES

1. A. Fujishima and K. Honda, *Nature*, 1972, **238**, 37-38.
2. C. Di Valentin, E. Finazzi, G. Pacchioni, A. Selloni, S. Livraghi, M. C. Paganini and E. Giamello, *Chem. Phys.*, 2007, **339**, 44-56.
3. X. Nie, S. Zhuo, G. Maeng and K. Sohlberg, *Int. J. Photoenergy*, 2009, **2009**, 22.
4. K. Yang, Y. Dai, B. Huang and M.-H. Whangbo, *J. Phys. Chem. C*, 2009, **113**, 2624-2629.
5. J. Yu, Q. Xiang and M. Zhou, *Appl. Catal., B*, 2009, **90**, 595-602.
6. J. W. Zheng, A. Bhattcahrayya, P. Wu, Z. Chen, J. Highfield, Z. Dong and R. Xu, *J. Phys. Chem. C*, 2010, **114**, 7063-7069.
7. A. M. Czoska, S. Livraghi, M. Chiesa, E. Giamello, S. Agnoli, G. Granozzi, E. Finazzi, C. D. Valentin and G. Pacchioni, *J. Phys. Chem. C*, 2008, **112**, 8951-8956.
8. P. Haowei, L. Jingbo, L. Shu-Shen and X. Jian-Bai, *J. Phys.: Condens. Matter*, 2008, **20**, 125207.
9. J.-M. Herrmann, *New J. Chem.*, 2012, **36**, 883-890.
10. T. Ikeda, T. Nomoto, K. Eda, Y. Mizutani, H. Kato, A. Kudo and H. Onishi, *J. Phys. Chem. C*, 2008, **112**, 1167-1173.
11. J.-P. Xu, L. Li, L.-Y. Lv, X.-S. Zhang, X.-M. Chen, J.-F. Wang, F.-M. Zhang, W. Zhong and Y.-W. Du, *Chin. Phys. Lett.*, 2009, **26**, 097502.
12. L. Wenxian, *Phys. Status Solidi RRL*, 2015, **9**, 10-27.
13. V. Etacheri, C. Di Valentin, J. Schneider, D. Bahnemann and S. C. Pillai, *J. Photochem. Photobiol. C: Photochem. Rev.*, 2015, **25**, 1-29.
14. S. Na Phattalung, S. Limpijumnong and J. Yu, *Appl. Catal., B*, 2017, **200**, 1-9.
15. C. D. Valentin, G. Pacchioni, H. Onishi and A. Kudo, *Chem. Phys. Lett.*, 2009, **469**, 166-171.
16. Y. Gai, J. Li, S. S. Li, J. B. Xia and S. H. Wei, *Phys. Rev. Lett.*, 2009, **102**, 036402.
17. R. Long and N. J. English, *J. Phys. Chem. C*, 2010, **114**, 11984-11990.
18. R. Long and N. J. English, *Chem. Mater.*, 2010, **22**, 1616-1623.
19. J. Zhang, C. Pan, P. Fang, J. Wei and R. Xiong, *ACS Appl. Mater. Interfaces*, 2010, **2**, 1173-1176.
20. W. Zhu, X. Qiu, V. Iancu, X.-Q. Chen, H. Pan, W. Wang, N. M. Dimitrijevic, T. Rajh, H. M. Meyer, M. P. Paranthaman, G. M. Stocks, H. H. Weitering, B. Gu, G. Eres and Z. Zhang, *Phys. Rev. Lett.*, 2009, **103**, 226401.
21. M. Grätzel, *J. Photochem. Photobiol. C: Photochem. Rev.*, 2003, **4**, 145-153.
22. W. Hou and S. B. Cronin, *Adv. Funct. Mater.*, 2013, **23**, 1612-1619.

23. M. Honda, Y. Kumamoto, A. Taguchi, Y. Saito and S. Kawata, *Appl. Phys. Lett.*, 2014, **104**, 061108.
24. S. Shuang, R. Lv, Z. Xie and Z. Zhang, *Sci. Rep.*, 2016, **6**, 26670.
25. S. Linic, P. Christopher and D. B. Ingram, *Nat. Mater.*, 2011, **10**, 911.
26. S. C. Warren and E. Thimsen, *Energy Environ. Sci.*, 2012, **5**, 5133-5146.
27. Q. Jin, M. Fujishima and H. Tada, *J. Phys. Chem. C*, 2011, **115**, 6478-6483.
28. H. Tada, Q. Jin, A. Iwaszuk and M. Nolan, *J. Phys. Chem. C*, 2014, **118**, 12077-12086.
29. J. A. Libera, J. W. Elam, N. F. Sather, T. Rajh and N. M. Dimitrijevic, *Chem. Mater.*, 2010, **22**, 409-413.
30. M. Nolan, *Phys. Chem. Chem. Phys.*, 2011, **13**, 18194-18199.
31. M. Fronzi, W. Daly and M. Nolan, *Appl. Catal., A*, 2016, **521**, 240-249.
32. M. Nolan, A. Iwaszuk, A. K. Lucid, J. J. Carey and M. Fronzi, *Adv. Mater.*, 2016, **28**, 5425-5446.
33. M. Fronzi, A. Iwaszuk, A. Lucid and M. Nolan, *J. Phys.: Condens. Matter*, 2016, **28**, 074006.
34. M. Nolan, A. Iwaszuk and K. A. Gray, *J. Phys. Chem. C*, 2014, **118**, 27890-27900.
35. A. Lucid, A. Iwaszuk and M. Nolan, *Mater. Sci. Semicond. Process.*, 2014, **25**, 59-67.
36. A. Iwaszuk and M. Nolan, *Catal. Sci. Technol.*, 2013, **3**, 2000-2008.
37. A. Iwaszuk and M. Nolan, *J. Mater. Chem. A*, 2013, **1**, 6670-6677.
38. A. Iwaszuk, P. A. Mulheran and M. Nolan, *J. Mater. Chem. A*, 2013, **1**, 2515-2525.
39. A. Iwaszuk, M. Nolan, Q. Jin, M. Fujishima and H. Tada, *J. Phys. Chem. C*, 2013, **117**, 2709-2718.
40. M. Nolan, *ACS Appl. Mater. Interfaces*, 2012, **4**, 5863-5871.
41. M. Nolan, *Chem. Commun.*, 2011, **47**, 8617-8619.
42. J. B. Park, J. Graciani, J. Evans, D. Stacchiola, S. D. Senanayake, L. Barrio, P. Liu, J. F. Sanz, J. Hrbek and J. A. Rodriguez, *J. Am. Chem. Soc.*, 2010, **132**, 356-363.
43. A. Iwaszuk and M. Nolan, *Phys. Chem. Chem. Phys.*, 2011, **13**, 4963-4973.
44. Q. Jin, M. Fujishima, M. Nolan, A. Iwaszuk and H. Tada, *J. Phys. Chem. C*, 2012, **116**, 12621-12626.
45. S. J. A. Moniz, S. A. Shevlin, X. An, Z.-X. Guo and J. Tang, *Chem. Eur. J.*, 2014, **20**, 15571-15579.
46. J. Graciani, K. Mudiyanselage, F. Xu, A. E. Baber, J. Evans, S. D. Senanayake, D. J. Stacchiola, P. Liu, J. Hrbek, J. F. Sanz and J. A. Rodriguez, *Science*, 2014, **345**, 546-550.
47. Y. Wang, J. Zhao, T. Wang, Y. Li, X. Li, J. Yin and C. Wang, *J. Catal.*, 2016, **337**, 293-302.
48. J. Graciani, J. J. Plata, J. F. Sanz, P. Liu and J. A. Rodriguez, *J. Chem. Phys.*, 2010, **132**, 104703.
49. J. B. Park, J. Graciani, J. Evans, D. Stacchiola, S. Ma, P. Liu, A. Nambu, J. F. Sanz, J. Hrbek and J. A. Rodriguez, *Proc. Natl. Acad. Sci. U.S.A.*, 2009, **106**, 4975-4980.
50. A. C. Johnston-Peck, S. D. Senanayake, J. J. Plata, S. Kundu, W. Xu, L. Barrio, J. Graciani, J. F. Sanz, R. M. Navarro, J. L. G. Fierro, E. A. Stach and J. A. Rodriguez, *J. Phys. Chem. C*, 2013, **117**, 14463-14471.
51. C. L. Muhich, B. D. Ehrhart, I. Al-Shankiti, B. J. Ward, C. B. Musgrave and A. W. Weimer, *Wiley Interdisciplinary Reviews: Energy and Environment*, 2016, **5**, 261-287.
52. Y.-F. Li and Z.-P. Liu, *Wiley Interdiscip. Rev. Comput. Mol. Sci.*, 2016, **6**, 47-64.
53. Y. Cheng and S. P. Jiang, *Prog. Nat. Sci. Mater. Int.*, 2015, **25**, 545-553.
54. Á. Valdés, Z. W. Qu, G. J. Kroes, J. Rossmeisl and J. K. Nørskov, *J. Phys. Chem. C*, 2008, **112**, 9872-9879.
55. A. V. Bandura, D. G. Sykes, V. Shapovalov, T. N. Troung, J. D. Kubicki and R. A. Evarestov, *J. Phys. Chem. B*, 2004, **108**, 7844-7853.
56. D. Fernández-Torre, K. Kośmider, J. Carrasco, M. V. Ganduglia-Pirovano and R. Pérez, *J. Phys. Chem. C*, 2012, **116**, 13584-13593.
57. M. Fronzi, S. Piccinin, B. Delley, E. Traversa and C. Stampfl, *Phys. Chem. Chem. Phys.*, 2009, **11**, 9188-9199.
58. H. Zhang, P. Zhou, Z. Chen, W. Song, H. Ji, W. Ma, C. Chen and J. Zhao, *J. Phys. Chem. C*, 2017, **121**, 2251-2257.
59. C. Sun, L.-M. Liu, A. Selloni, G. Q. Lu and S. C. Smith, *J. Mater. Chem.*, 2010, **20**, 10319-10334.

60. Y.-F. Li and A. Selloni, *ACS Catal.*, 2016, **6**, 4769-4774.
61. N. Tymińska, G. Wu and M. Dupuis, *J. Phys. Chem. C*, 2017, **121**, 8378-8389.
62. M.-T. Nguyen, S. Piccinin, N. Seriani and R. Gebauer, *ACS Catal.*, 2015, **5**, 715-721.
63. J. Cheng, J. VandeVondele and M. Sprik, *J. Phys. Chem. C*, 2014, **118**, 5437-5444.
64. D. Wang, H. Wang and P. Hu, *Phys. Chem. Chem. Phys.*, 2015, **17**, 1549-1555.
65. X. Chen, S. N. Choing, D. J. Aschaffenburg, C. D. Pemmaraju, D. Prendergast and T. Cuk, *J. Am. Chem. Soc.*, 2017, **139**, 1830-1841.
66. X. Chang, T. Wang and J. Gong, *Energy Environ. Sci.*, 2016, **9**, 2177-2196.
67. V. P. Indrakanti, *Fuel Process. Technol.*, 2011, **v. 92**, pp. 805-811-2011 v.2092 no.2014.
68. W. Pipornpong, R. Wanbayor and V. Ruangpornvisuti, *Appl. Surf. Sci.*, 2011, **257**, 10322-10328.
69. W.-J. Yin, B. Wen, S. Bandaru, M. Krack, M. W. Lau and L.-M. Liu, *Sci. Rep.*, 2016, **6**, 23298.
70. C.-T. Yang, B. C. Wood, V. R. Bhethanabotla and B. Joseph, *J. Phys. Chem. C*, 2014, **118**, 26236-26248.
71. R. J. Walker, A. Pougin, F. E. Oropeza, I. J. Villar-Garcia, M. P. Ryan, J. Strunk and D. J. Payne, *Chem. Mater.*, 2016, **28**, 90-96.
72. E. L. Uzunova, N. Seriani and H. Mikosch, *Phys. Chem. Chem. Phys.*, 2015, **17**, 11088-11094.
73. A. K. Mishra, A. Roldan and N. H. d. Leeuw, *J. Chem. Phys.*, 2016, **145**, 044709.
74. A. K. Mishra, A. Roldan and N. H. de Leeuw, *J. Phys. Chem. C*, 2016, **120**, 2198-2214.
75. H. Wu, N. Zhang, H. Wang and S. Hong, *Chem. Phys. Lett.*, 2013, **568**, 84-89.
76. L. I. Bendavid and E. A. Carter, *J. Phys. Chem. C*, 2013, **117**, 26048-26059.
77. H. Wu, N. Zhang, Z. Cao, H. Wang and S. Hong, *Int. J. Quantum Chem*, 2012, **112**, 2532-2540.
78. M. Behrens, F. Studt, I. Kasatkin, S. Kühl, M. Hävecker, F. Abild-Pedersen, S. Zander, F. Girgsdies, P. Kurr, B.-L. Kniep, M. Tovar, R. W. Fischer, J. K. Nørskov and R. Schlögl, *Science*, 2012, **336**, 893-897.
79. W. J. Durand, A. A. Peterson, F. Studt, F. Abild-Pedersen and J. K. Nørskov, *Surf. Sci.*, 2011, **605**, 1354-1359.
80. L. C. Grabow and M. Mavrikakis, *ACS Catal.*, 2011, **1**, 365-384.
81. G. Kresse and J. Hafner, *Phys. Rev. B.*, 1994, **49**, 14251-14269.
82. J. Furthmüller, J. Hafner and G. Kresse, *Phys. Rev. B.*, 1996, **53**, 7334-7351.
83. P. E. Blöchl, *Phys. Rev. B.*, 1994, **50**, 17953-17979.
84. G. Kresse and D. Joubert, *Phys. Rev. B.*, 1999, **59**, 1758-1775.
85. J. P. Perdew, K. Burke and M. Ernzerhof, *Phys. Rev. Lett.*, 1996, **77**, 3865-3868.
86. V. I. Anisimov, J. Zaanen and O. K. Andersen, *Phys. Rev. B.*, 1991, **44**, 943-954.
87. S. L. Dudarev, G. A. Botton, S. Y. Savrasov, C. J. Humphreys and A. P. Sutton, *Phys. Rev. B.*, 1998, **57**, 1505-1509.
88. B. J. Morgan and G. W. Watson, *Surf. Sci.*, 2007, **601**, 5034-5041.
89. D. A. Andersson, S. I. Simak, B. Johansson, I. A. Abrikosov and N. V. Skorodumova, *Phys. Rev. B.*, 2007, **75**, 035109.
90. H. P. Boehm, *Discuss. Faraday Soc.*, 1971, **52**, 264-275.
91. G. E. Brown, V. E. Henrich, W. H. Casey, D. L. Clark, C. Eggleston, A. Felmy, D. W. Goodman, M. Grätzel, G. Maciel, M. I. McCarthy, K. H. Nealson, D. A. Sverjensky, M. F. Toney and J. M. Zachara, *Chem. Rev.*, 1999, **99**, 77-174.
92. G. Henkelman, A. Arnaldsson and H. Jónsson, *Comput. Mater. Sci.*, 2006, **36**, 354-360.
93. C. Di Valentin and A. Selloni, *J. Phys. Chem. Lett.*, 2011, **2**, 2223-2228.
94. A. Iwaszuk and M. Nolan, *J. Phys. Chem. C*, 2011, **115**, 12995-13007.
95. A. R. Albuquerque, A. Bruix, I. M. G. dos Santos, J. R. Sambrano and F. Illas, *J. Phys. Chem. C*, 2014, **118**, 9677-9689.
96. A. R. Albuquerque, A. Bruix, J. R. Sambrano and F. Illas, *J. Phys. Chem. C*, 2015, **119**, 4805-4816.
97. J. Gan, X. Lu, J. Wu, S. Xie, T. Zhai, M. Yu, Z. Zhang, Y. Mao, S. C. I. Wang, Y. Shen and Y. Tong, *Sci. Rep.,* 2013, **3**, 1021.
98. L. Liu, C. Zhao and Y. Li, *J. Phys. Chem. C*, 2012, **116**, 7904-7912.

99. Y.-X. Pan, Z.-Q. Sun, H.-P. Cong, Y.-L. Men, S. Xin, J. Song and S.-H. Yu, *Nano Res.*, 2016, **9**, 1689-1700.
100. S. Huygh, A. Bogaerts and E. C. Neyts, *J. Phys. Chem. C*, 2016, **120**, 21659-21669.
101. Z. Cheng, B. J. Sherman and C. S. Lo, *J. Chem. Phys.*, 2013, **138**, 014702.
102. X. Lu, W. Wang, S. Wei, C. Guo, Y. Shao, M. Zhang, Z. Deng, H. Zhu and W. Guo, *RSC Adv.*, 2015, **5**, 97528-97535.
103. A. B. Vidal, L. Feria, J. Evans, Y. Takahashi, P. Liu, K. Nakamura, F. Illas and J. A. Rodriguez, *J. Phys. Chem. Lett.*, 2012, **3**, 2275-2280.
104. S. Posada-Perez, F. Vines, P. J. Ramirez, A. B. Vidal, J. A. Rodriguez and F. Illas, *Phys. Chem. Chem. Phys.*, 2014, **16**, 14912-14921.
105. C. Liu, T. R. Cundari and A. K. Wilson, *J. Phys. Chem. C*, 2012, **116**, 5681-5688.
106. J. B. Park, J. Graciani, J. Evans, D. Stacchiola, S. D. Senanayake, L. Barrio, P. Liu, J. F. Sanz, J. Hrbek and J. A. Rodriguez, *J. Am. Chem. Soc.*, 2009, **132**, 356-363.
107. Z. Yang, L. Xie, D. Ma and G. Wang, *J. Phys. Chem. C*, 2011, **115**, 6730-6740.
108. S. Fuente, M. M. Branda and F. Illas, *Theor. Chem. Acc.*, 2012, **131**, 1190.
109. M. Molinari, S. C. Parker, D. C. Sayle and M. S. Islam, *J. Phys. Chem. C*, 2012, **116**, 7073-7082.
110. D. Marrocchelli and B. Yildiz, *J. Phys. Chem. C*, 2012, **116**, 2411-2424.
111. D. R. Mullins, P. M. Albrecht, T.-L. Chen, F. C. Calaza, M. D. Biegalski, H. M. Christen and S. H. Overbury, *J. Phys. Chem. C*, 2012, **116**, 19419-19428.
112. J. Carrasco, D. López-Durán, Z. Liu, T. Duchoň, J. Evans, S. D. Senanayake, E. J. Crumlin, V. Matolín, J. A. Rodríguez and M. V. Ganduglia-Pirovano, *Angew. Chem. Int. Ed.*, 2015, **54**, 3917-3921.
113. J. Fan, B. Xu, J. Z. Zhao and H. Xu, *Phys. Chem. Chem. Phys.*, 2018, DOI: 10.1039/C7CP06117J.

CO_2 and Water Activation on Ceria Nanocluster Modified TiO_2 Rutile (110)

Stephen Rhatigan and Michael Nolan*

Tyndall National Institute, University College Cork, Lee Maltings, Cork, Ireland

michael.nolan@tyndall.ie

Supplementary Material

This document contains supplementary material relevant to the paper entitled: *"CO_2 and Water activation on Ceria Nanocluster Modified TiO_2 Rutile (110)"*.

List of Tables:

List of Figures:

Table S1. Computed oxygen vacancy formation energies for each O site of the supported ceria nanoclusters. The most stable vacancy sites are highlighted in bold.

Ce_5O_{10}-rutile-(110)		Ce_5O_9-rutile-(110)	
O site	**E_{vac} (eV)**	**O site**	**E_{vac} (eV)**
1	1.35	1	2.96
2	2.03	2	2.95
3	1.38	3	1.86
4	1.67	4	2.03
5	2.38	5	2.38
6	**0.18**	6	2.30
7	1.93	**7**	**1.48**
8	1.53	8	1.76
9	1.56	9	2.35
10	1.65		

Ce_6O_{12}-rutile-(110)		Ce_6O_{11}-rutile-(110)		Ce_6O_{10}-rutile-(110)	
O site	**E_{vac} (eV)**	**O site**	**E_{vac} (eV)**	**O site**	**E_{vac} (eV)**
1	1.91	1	1.56	1	2.15
2	1.68	2	1.49	2	2.97
3	-0.10	**3**	**-0.16**	3	3.35
4	1.68	4	1.60	4	1.98
5	1.26	5	1.03	5	2.60
6	1.62	6	1.72	6	2.02
7	0.58	7	1.56	7	2.68
8	2.81	8	2.49	8	2.89
9	3.09	9	2.01	**9**	**0.30**
10	0.29	10	0.14	10	5.04
11	**-0.46**	11	2.40		
12	2.70				

Table S2. Ce-O distances and coordination for each of the Ce ions in the supported nanoclusters in the stoichiometric, ground state and reduced state. Reduced Ce^{3+} ions are highlighted in bold.

Stoichiometry	**Ion**	**Coord**	**Ce-O distances (Å)**					
Ce_5O_{10}	Ce_I	5	2.42	2.24	2.19	2.17	2.14	
	Ce_{II}	5	2.38	2.31	2.31	2.17	2.15	
	Ce_{III}	4	2.29	2.12	2.11	2.08		
	Ce_{IV}	5	2.44	2.29	2.24	2.16	2.15	
	Ce_V	4	2.24	2.15	2.13	2.08		
Ce_5O_9	**Ce_I**	6	2.59	2.57	2.54	2.45	2.33	2.31
	Ce_{II}	5	2.42	2.35	2.31	2.14	2.13	
	Ce_{III}	4	2.34	2.15	2.14	2.01		
	Ce_{IV}	5	2.60	2.42	2.40	2.29	2.25	
	Ce_V	4	2.25	2.14	2.12	2.08		
Ce_5O_8	**Ce_I**	5	2.57	2.56	2.40	2.29	2.22	
	Ce_{II}	5	2.54	2.53	2.38	2.31	2.25	
	Ce_{III}	4	2.34	2.13	2.09	2.07		
	Ce_{IV}	4	2.47	2.43	2.33	2.17		
	Ce_V	3	2.24	2.17	2.16			
Stoichiometry	**Ion**	**Coord**	**Ce-O distances (Å)**					
Ce_6O_{12}	Ce_I	5	2.46	2.41	2.39	2.38	1.86	
	Ce_{II}	5	2.52	2.37	2.36	2.35	1.86	
	Ce_{III}	4	2.19	2.19	2.13	2.07		
	Ce_{IV}	5	2.35	2.22	2.20	2.20	2.15	
	Ce_V	6	2.45	2.41	2.37	2.24	2.24	2.2
	Ce_{VI}	5	2.57	2.54	2.42	2.33	1.85	
Ce_6O_{10}	**Ce_I**	4	2.35	2.32	2.26	2.23		
	Ce_{II}	5	2.49	2.36	2.36	2.34	1.88	
	Ce_{III}	4	2.35	2.32	2.26	2.23		
	Ce_{IV}	5	2.48	2.36	2.31	2.30	2.28	
	Ce_V	6	2.48	2.48	2.45	2.21	2.16	2.16
	Ce_{VI}	6	2.58	2.58	2.55	2.36	2.36	2.31
Ce_6O_9	**Ce_I**	4	2.31	2.29	2.28	2.26		
	Ce_{II}	4	2.32	2.28	2.28	2.25		
	Ce_{III}	4	2.29	2.29	2.29	2.29		
	Ce_{IV}	5	2.48	2.41	2.34	2.28	2.28	
	Ce_V	6	2.57	2.56	2.51	2.34	2.33	2.32
	Ce_{VI}	6	2.60	2.58	2.56	2.37	2.33	2.32

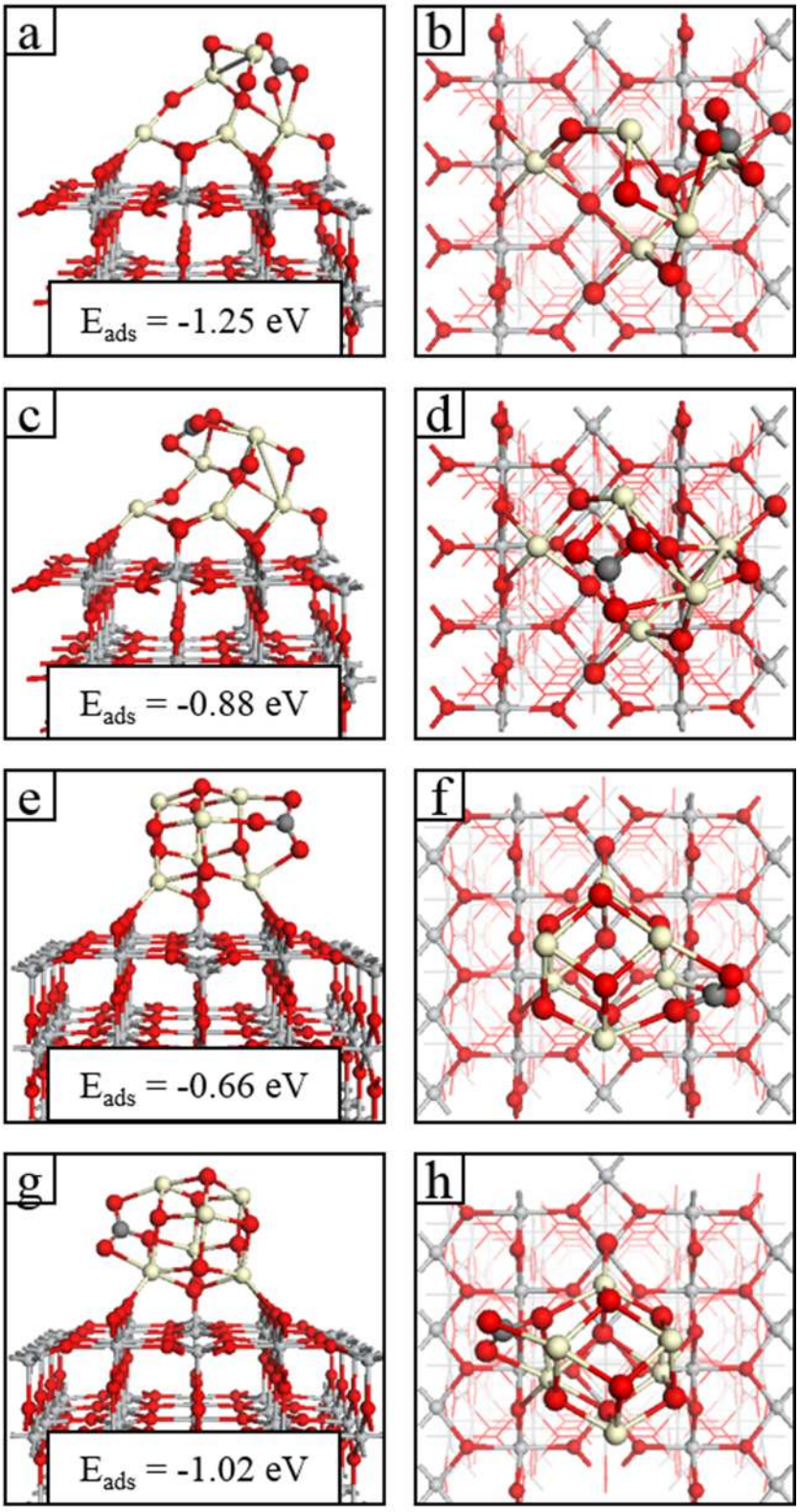

Figure S1. Relaxed atomic structure for stable configurations of CO_2 adsorbed at **(a)**, **(b)**, **(c)** and **(d)** Ce_5O_8-rutile-(110) and **(e)**, **(f)**, **(g)** and **(h)** Ce_6O_9-rutile-(110). Panels on the left show side views, panels on the right show top views. Insets of panels on the left show the adsorption energies. Colour code: Ti, grey; O, red; Ce, cream; C, dark grey.

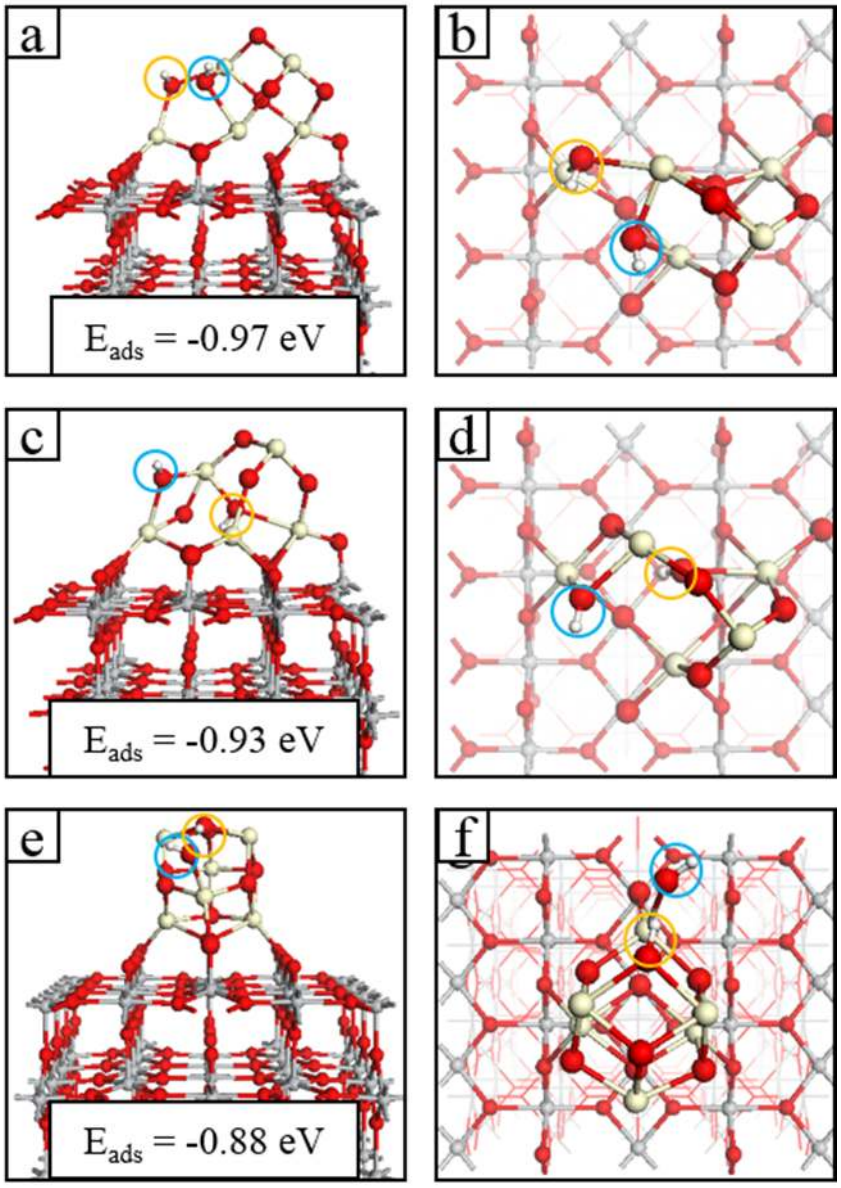

Figure S2. Relaxed atomic structure for stable configurations of H_2O adsorbed at **(a)**, **(b)**, **(c)** and **(d)** Ce_5O_8-rutile-(110) and **(e)** and **(f)** Ce_6O_9-rutile-(110). Panels on the left show side views, panels on the right show top views. Insets of panels on the left show the adsorption energies. Colour code: Ti, grey; O, red; Ce, cream; H, white.